Metal oxidation prevention of low carbon steel in acidic medium: synthesis, electrochemical, and theoretical studies of a novel di-cationic pyridinium surfactant

G. Gece,[1]* S. Öztürk[2] and G. Akgül[2]

[1]*Department of Chemistry, Faculty of Engineering and Natural Sciences, Bursa Technical University, Bursa, 16310 Turkey*
[2]*Department of Chemistry, Faculty of Science and Arts, Bursa Uludag University, Bursa, 16059 Turkey*
**E-mail: gokhangc@gmail.com*

Abstract

Low carbon steels are widely used industrially, especially in the automotive and construction sectors. The corrosion rates of these metals in acidic environments are generally very fast and it is of particular importance to prevent metal corrosion in this environment. For this reason, in this study, di-cationic surfactant containing two pyridinium nitrogen with corrosion inhibitory potential, named 1-dodecyl-2-(11-(pyridin-1-ium-1-yl)undecanamido)pyridin-1-ium di-bromide (DPUP), was synthesized. The structure of this compound was elucidated by spectroscopic methods (FT-IR and NMR) and electrochemical measurement methods (potentiodynamic polarization and electrochemical impedance spectroscopy) were preferred to determine the corrosion inhibition activities at different concentrations (2, 10 and 50 ppm) at room temperature (25°C). The lowest corrosion rate and the highest corrosion inhibition efficiency were obtained at an inhibitor concentration of 50 ppm. In order to understand whether this new compound was adsorbed on the metal surface, and thereby making the surface hydrophobic, contact angle measurement was performed using the drop method. Adsorption isotherm studies were performed to determine the predominant type of adsorption (physical or chemical) of the compound adsorbed on the steel surface and it was found to be in accordance with Langmuir. In addition, SEM + EDX analysis was performed on the metal surfaces to visually support that the metal is protected against corrosion and theoretical calculations were carried out using Density Functional Theory (DFT) method.

Received: August 6, 2025. Published: November 10, 2025 doi: 10.17675/2305-6894-2025-14-4-16

Keywords: *di-cationic pyridinium surfactant, carbon steel, electrochemical impedance spectroscopy, DFT.*

1. Introduction

Mild steel is widely used in various environmental mediums due to its affordability, strength, and versatility. It is commonly used in the construction of buildings, bridges, and other infrastructure projects. Its strength and durability make it ideal for structural components

that need to withstand environmental factors such as wind, earthquakes, and varying temperatures [1]. In the transportation sector, mild steel is used in the manufacturing of vehicles, ships, and trains. Its ability to be easily welded and formed into different shapes makes it suitable for creating robust and reliable transportation equipment [1]. Mild steel is also often used for pipelines and storage tanks in the oil and gas industry. Its strength and resistance to pressure make it suitable for transporting and storing various fluids, including water, oil, and gas [2]. Despite its many advantages, mild steel is prone to corrosion, especially in acidic or saline environments. This can lead to structural degradation and failure if not properly managed. To mitigate this, various corrosion inhibitors and protective coatings are applied to extend the lifespan of mild steel structures [2, 3]. Recent studies have focused on using environmentally friendly corrosion inhibitors derived from natural sources. These green inhibitors are less toxic and more sustainable compared to traditional synthetic inhibitors, making them a better choice for protecting mild steel in environmental applications [2, 3]. Overall, mild steel remains a popular choice in many industries due to its cost-effectiveness and mechanical properties, despite the challenges posed by corrosion. Corrosion is the deterioration of materials as a result of chemical or electrochemical reactions with their environment and this process can lead to serious economic and structural problems in various sectors [4]. Corrosion causes billions of dollars in economic losses worldwide. These losses are caused by material replacement, maintenance and repair costs, and production interruptions. Corrosion shortens the life of materials, requiring more frequent replacement. This has negative impacts both economically and environmentally. Corrosion poses safety risks by weakening the structural integrity of structures and machinery. Especially in critical infrastructure such as bridges, pipelines and airplanes, corrosion can lead to serious accidents. Corrosion can also cause efficiency losses in power generation and distribution systems. Leaks in power plants and pipelines due to corrosion lead to energy losses [5].

Pyridinium cationic surfactants are a fascinating class of compounds that have garnered significant attention in both industrial and academic research. These surfactants, characterized by their positively charged pyridinium head groups, exhibit unique properties that make them invaluable in various applications, from antimicrobial agents to fabric softeners. Their ability to reduce surface tension and form micelles is crucial in processes such as emulsification and solubilization [6, 7]. Pyridinium cationic surfactants are known for their effective anti-corrosion properties, which make them valuable in various industrial applications. The anti-corrosion effect of pyridinium cationic surfactants is due to their ability to form a stable, protective layer on metal surfaces, reducing the interaction with corrosive agents and inhibiting electrochemical reactions. This makes them highly effective in extending the lifespan of metal components in various industrial settings [8]. Literature studies on pyridinium di-cationic surfactants as anti-corrosion agents have shown promising results in various applications. These surfactants are particularly effective in acidic environments, where they form a protective layer on metal surfaces, preventing corrosion. Research has focused on synthesizing pyridinium di-cationic surfactants with different

functional groups attached to the pyridinium nitrogen. For example, Akgül and Öztürk 2023 [9], synthesized two cationic surfactants with amide and ester groups, respectively, and evaluated their corrosion inhibition properties in 1.0 M HCl. The results indicated that both surfactants provided significant protection, with the ester-functionalized surfactant showing slightly better performance at low inhibitor concentrations [9]. In another study, techniques such as Tafel polarization, linear polarization resistance (LPR) and electrochemical impedance spectroscopy (EIS) were used to evaluate the corrosion inhibition efficiency of pyridinium-based surfactants. In this research, *N*-(*n*-octyl)-3-methylpyridinium bromide (Py8) and *N*-(*n*-dodecyl)-3-methylpyridinium bromide (Py12) were tested for their ability to protect EN3B mild steel in acidic chloride media. The maximum inhibition efficiencies obtained were 85% and 82% respectively. Density functional theory (DFT) calculations have also been used to support experimental findings, highlighting the importance of alkyl chain length and intramolecular charge transfer in determining the inhibition performance [10]. In these two studies, the adsorption behavior of the surfactants on metal surfaces often follows the Langmuir adsorption isotherm, indicating strong interactions between the surfactant molecules and the metal surface. This strong adsorption is crucial for forming an effective protective layer [9, 10]. These studies underscore the potential of pyridinium di-cationic surfactants as effective anti-corrosion agents, particularly in harsh acidic environments [11].

Computational chemistry methods are becoming omnipresent in corrosion inhibitor efficiency prediction [12]. Geometry optimization of the inhibitors within the chosen route can be performed using a myriad of approaches, including DFT. Further detailed molecular modelling studies provide additional understanding toward a robust correlation between a calculated parameter and corrosion efficiency. By unifying the experimental and computational treatments, accurate estimation of the inhibition behaviour of the potential compounds could be anticipated [13].

In this study, a pyridinium surfactant class substance, which generally shows high corrosion inhibition, will be synthesized and its inhibition efficiency will be investigated by electrochemical methods. The substance to be synthesized will be a positively charged di-cationic surfactant with long chain alkyl groups attached to two pyridinium nitrogen. Electrochemical impedance spectroscopy (EIS) and potentiodynamic polarization techniques will be used to determine the corrosion inhibition efficiency. These measurements will be carried out in 1.0 M HCl solution. Metal electrodes will be immersed in solutions with and without inhibitors and their corrosion rates will be determined. Contact angle measurements and adsorption isotherm studies will be carried out to investigate whether the inhibitor adsorbs on the metal surface and protects it against corrosion in acidic environment and which type of adsorption is dominant. In addition, scanning electron microscopy (SEM) and AFM analysis will be used to determine the morphological changes and surface roughness ratios of the metal surfaces, respectively.

2. Materials and Experimental Procedures

2.1. Materials and instrumentations

11-Bromoundecanoic acid, thionyl chloride ($SOCl_2$), toluene, 2-amino-pyridine, chloroform, acetonitrile, 1-dodecyl bromide, pyridine and 37% HCl chemicals and solvents were purchased from Merck (Merck, Darmstadt, Germany). Reagent named triethylamine (TEA) was obtained from Sigma-Aldrich company (St. Louis, MO, USA). These reagents and solvents were used without further purification. Thin layer chromatography (TLC) was performed using silica gel (60 F254, Merck, Darmstadt, Germany) plates. Perkin Elmer Spectrum Two FT-IR spectrophotometer (Shelton, Connecticut, USA) and Agilent 600 MHz Premium Compact NMR spectrometer (Santa Clara, CA, USA) in DMSO (Dimethylsulfoxide) solvent were used to obtain the FT-IR and NMR spectra (^{1}H NMR and ^{13}C NMR) of the synthesized di-cationic surfactant. A NUVE EV 018 vacuum oven (Ankara, Turkiye) was used to dry the metal plates to constant weight, excluding atmospheric air. A LECO CHNS-932 elemental analyzer (Saint Joseph, MI, USA) was used for elemental content determination.

2.2. Description of synthesis

In the first stage, 11-bromo-undecanoyl chloride ($Br(CH_2)_{10}CO_2Cl$) was obtained through the reaction between thionyl chloride ($SOCl_2$) and 11-bromoundecanoic acid ($C_{11}H_{21}BrO_2$) with toluene as solvent. Thereafter, $Br(CH_2)_{10}CO_2Cl$ reacted with 2-aminopyridine in the presence of triethylamine and chloroform. As a result of the reaction, the acid chloride compound was converted into amide compound (**1**). By heating compound **1** at 150°C for 24 h in acetonitrile (CH_3CN) containing 1-dodecyl bromide, compounds **2** were produced (Scheme 1).

*2.2.1. 1-Dodecyl-2-(11-(pyridin-1-ium-1-yl)undecanamido)pyridin-1-ium dibromide (DPUP) ($C_{33}H_{55}Br_2N_3O$) (**3**)*

The same molar ratio (5.01 mmol) of compound **2**, pyridine and 30 mL ethanol as solvent was added to the reaction flask. The reaction mixture was boiled for 48 hours under a reflux condenser. The progress of the reaction was monitored by TLC. At the end of the time, the ethanol was evaporated in an evaporator and the residue was washed in a mixture of acetone-diethyl ether (approximately 1–4). At the end of the washing process, a brown, oily wax-like product was obtained which was well soluble in water. Yield = 2.34 g (70%).

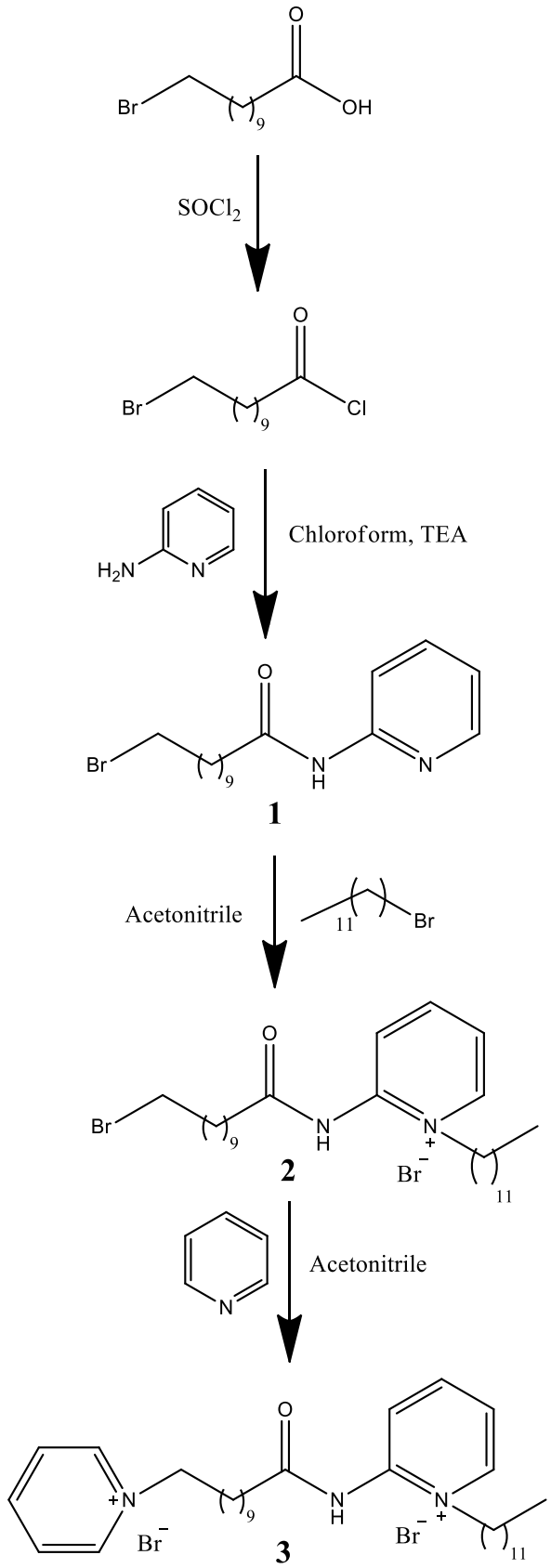

Scheme 1. Reaction steps of DPUP (3).

2.3. Corrosion tests to determine the effectiveness against metal oxidation in 1 M HCl environment

2.3.1. Metal plates used in corrosion tests and their preparation

The corrosion tests in acidic environments used metal plates made of low-carbon, cold-rolled steel. For the corrosion tests in acidic environments, the steel material was prepared according to DIN EN 10130 [14] and comprised 0.07% carbon, 0.35% manganese, 0.015% phosphorus, 0.015% sulfur, with the remainder being iron. For the corrosion tests in acidic environments, rectangular metal plates measuring 0.1 cm in thickness, 2.2 cm in width, and 5.0 cm in length were utilized. The preparation of these metals followed the method described by Öztürk in 2018 [15]. To remove any rust and oxide layers, the plates were immersed in a 15% HCl solution for 5 minutes. The metal coupons were cleaned using distilled water. After drying, the metal plates were smoothed with sandpaper of varying grits (320, 800, and 1500). Subsequently, they were soaked in acetone for a period of time. After being removed from the acetone, the metal plates were dried in a NUVE EV 018 vacuum oven (Ankara, Turkiye).

2.3.2. Electrochemical measurement methods

In this study, we performed electrochemical corrosion tests on our samples, such as Open Circuit Potential (OCP), Tafel Extrapolation, and EIS, using the VersaSTAT 4 galvanostat/potentiostat device (TN, USA). VersaStudio software was employed for the Potentiodynamic Polarization (PDP) experiments [16]. Electrochemical measurements were conducted using a standard three-electrode electrochemical cell. The working electrode was a prepared metal plate conforming to DIN EN 10130 standards. Before the corrosion test, the surface of the metal plate intended for exposure was sanded with different grades of emery paper, degreased with acetone, rinsed with ultrapure water, and then dried. The metal plate, acting as the working electrode, was covered with polyimide kapton tape, exposing only a 1.0 cm^2 area to the solution. The working electrode was a prepared metal plate conforming to DIN EN 10130 standards. Before the corrosion test, the surface of the metal plate intended for exposure was sanded with different grades of emery paper, degreased with acetone, rinsed with ultrapure water, and then dried. The metal plate, acting as the working electrode, was covered with polyimide kapton tape, exposing only a 1.0 cm^2 area to the solution. A saturated calomel electrode (SCE) was utilized as the reference electrode, and a platinum plate was used as the counter electrode. The experiments were carried out at a constant temperature of 25±1°C [17]. The system was monitored for an hour to ensure stabilization before taking measurements. Potentiodynamic polarization measurements were conducted after 3600 seconds of OCP measurements, with data points recorded every 0.5 seconds. Each test was repeated twice under the same conditions, and the data were analyzed using VersaStudio software. During the PDP experiments, the steel surface was scanned at a rate of 5 mV/s, maintaining a constancy criterion of 4.5 μV/s, within a range of −200 to +200 mV (*vs*. OCP) relative to the corrosion potential (E_{corr}). This was performed

in both the inhibitor-free solution and solutions containing 2, 10, and 50 ppm of the inhibitor. The polarization parameters related to the corrosion process were obtained by extrapolating the linear segments of the anodic and cathodic branches of the polarization curves. Corrosion current density (i_{corr}), E_{corr}, and the ability of the inhibitor to reduce the corrosion rate were obtained from these measurements. The measurement results were plotted on Tafel axes (log current density *vs*. potential), and corrosion parameters were derived from these graphs.

EIS data were used to determine the effects of inhibitor concentrations on corrosion. EIS measurements were taken over a wide frequency range (100 kHz–0.01 Hz) and presented as Nyquist diagrams. The evaluation of the obtained EIS data and the determination of circuit elements double-layer capacitance (C_{dl}), charge transfer resistance (R_{ct}), and solution resistance (R_s) were performed using ZsimpWin software. The data were modeled using commonly employed electrochemical circuit models, such as the Randles circuit.

2.4. Contact angle measurement method

Static pure water contact angles were measured at room temperature using a commercially available system. The contact angles on the surfaces of the metal stripes were determined with a KSV Attention Theta instrument from Hamburg, Germany. Prior to conducting contact angle measurements, the metal coupons were kept in a vacuum desiccator to avoid potential corrosion from air moisture. These coupons were tested for inhibition in an acidic medium at room temperature for durations of 6 and 24 hours. One metal plate was submerged in 100 mL of 1 M HCl solution without an inhibitor for 6 hours, while another plate was immersed for 24 hours. The metal plates were also immersed in HCl solutions with 50 ppm of the inhibitor DPUP (3) for 6 and 24 hours, respectively. Following this, the plates were removed from the acid solutions and dried in a vacuum desiccator to eliminate any remaining moisture. The contact angles of the surfaces were then measured using the sessile drop method. A syringe was utilized to dispense a single water droplet onto the metal stripe's surface. The contact angle was measured at both ends of the droplet placed on a thoroughly dry metal surface. Each water droplet, with a volume of 10 μL, was dispensed by the syringe. Contact angle values were determined for each droplet from 15 different photographs taken from various sections of the surfaces. The contact angles on the left and right sides of the droplet, where it touched the solid surface, were measured. The average of these two values was calculated to determine the overall contact angle. Subsequently, the mean and standard deviation of these measurements were computed [18].

2.5. SEM and EDX analysis method

To gain further insights into the corrosion process, Scanning Electron Microscopy (SEM) was utilized. After being removed from acid solutions, with or without inhibitors, and following the corrosion test based on the weight loss method, the metal sheets were cleaned, dried, and then examined. Surface images of the metals, magnified 1000 times, were

captured using a Carl Zeiss Gemini 300 SEM. Additionally, the chemical composition of the surfaces was analyzed using electron dispersive X-ray spectroscopy (EDX).

2.6. Theoretical method

To meliorate our percipience of the corrosion inhibition of DPUP (3) molecule, we implemented DFT calculations employing the B3LYP functional and the 6-311++G(d,p) basis set within Gaussian 09W software [20]. We explored the relation between corrosion inhibition effectiveness and electronic and structural properties through reactivity molecular descriptors, including the energy value of the highest occupied molecular orbital (E_{HOMO}), the energy value of the LUMO (E_{LUMO}), the HOMO–LUMO energy difference (ΔE), the ionization potential (I), the electronegativity (χ), the electron affinity (A), the global softness (σ), the global hardness (η), the global electrophilicity index (ω), nucleophilicity index (ε), electron accepting power (ω^{-}), electron donating power (ω^{+}), and the fraction of electrons transferred (ΔN). Each descriptor is calculated by the following equations defined within the scope of conceptual DFT;

$$\mu = \left(\frac{\partial E}{\partial N}\right)\cdot \nu(\vec{r}) \approx -\frac{(I+A)}{2} = \frac{E_{\mathrm{LUMO}} + E_{\mathrm{HOMO}}}{2} = \chi \tag{1}$$

$$\eta = \left(\frac{\partial^2 E}{\partial N^2}\right)\cdot \nu(\vec{r}) = \left(\frac{\partial \mu}{\partial N}\right) x_{\nu}(\vec{r}) = \frac{E_{\mathrm{LUMO}} - E_{\mathrm{HOMO}}}{2} \tag{2}$$

$$\sigma = (2\eta)^{-1} = \frac{1}{(I-A)} \tag{3}$$

$$\omega = \frac{\mu^2}{2\eta} = \frac{(I+A)^2}{4(I-A)} \approx \frac{(E_{\mathrm{LUMO}} + E_{\mathrm{HOMO}})^2}{4(E_{\mathrm{LUMO}} - E_{\mathrm{HOMO}})} \tag{4}$$

$$\varepsilon = \frac{1}{\omega} \tag{5}$$

$$\omega^{-} = \frac{(3I+A)^2}{16(I-A)} \tag{6}$$

$$\omega^{+} = \frac{(I+3A)^2}{16(I-A)} \tag{7}$$

$$\Delta N = \frac{\phi_{\mathrm{Fe}} - \chi_{\mathrm{inhibitor}}}{2(\eta_{\mathrm{Fe}} + \eta_{\mathrm{inhibitor}})} \tag{8}$$

where μ is the Lagrange multiplier associated with the normalization constraint of DFT identified as the electronic chemical potential, E is the total energy, and ν is the external potential. In agreement with Koopmans' theorem, I and A are the vertical ionization potential

and electron affinity of the system respectively, and given as $I=-E_{HOMO}$ and $A=-E_{LUMO}$, keeping the external potential fixed. In Eq. 8, the work function Φ presents the theoretical value of electronegativity of iron ($\Phi=\chi_{Fe}=4.82$ eV), and the global hardness corresponds to the metallic bulk ($\eta_{Fe}=0$ eV) [21].

3. Results and Discussion

3.1. Synthesis and spectroscopic analysis of DPUP (3)

The novel di-cationic surfactant (DPUP), which is studied as a corrosion inhibitor, was synthesized in four reaction steps (see Scheme 1). The characterization results of the synthesized surfactant are given in Table 1, respectively. It is possible to explain the characteristic peak values seen in the spectra as follows. In the FT-IR spectrum given in Figure 1, the peak at 3300 cm^{-1} is the amide N–H bond stretching, the peak at 3088 cm^{-1} is the aromatic C–H stretching belonging to the pyridinium at the left end, and the peak at 3061 cm^{-1} is the aromatic C–H stretching belonging to the amide bonded pyridinium group. The peaks at 2924 cm^{-1} and 2854 cm^{-1} belong to the aliphatic C–H stretching, the peak at 1662 cm^{-1} belongs to the C=O stretching in carbonyl on the amide bond and finally the peak at 1432 cm^{-1} belongs to the C–N stretching on the amide bond. As seen in the proton NMR spectrum (Figure 2), the peak at approximately 10.52 ppm belongs to the hydrogen in the N–H bond of the amide functional group; peaks at 9.19, 8.14, 7.94 and 7.76 ppm belong to the hydrogens of the C–H bond in the pyridinium ring to which the amide functional group is attached; peaks at 9.02, 7.99 and 7.83 ppm belong to the hydrogens of the C–H bond in the pyridinium ring at the end. Apart from these, peaks belonging to the hydrogens of the CH_2 group attached to the positively charged nitrogen atom in the pyridinium ring attached to the amide functional group at 4.63 ppm; hydrogens of the CH_2 group attached to the pyridinium nitrogen at 4.17 ppm; and hydrogens of the CH_2 group adjacent to the amide carbonyl (C=O) group at 2.47 ppm are observed. Finally, peaks belonging to the underlined hydrogens of $CH_3–C\underline{H}_2$, $O=C–NH–PyN^+–CH_2–C\underline{H}_2$, $C\underline{H}_2–CH_2–C=O$ and $C\underline{H}_3$ groups appeared at 2.34, 1.86, 1.61 and 0.77 ppm, respectively. In the C-NMR spectrum of the same substance given in Figure 3, the peak belonging to the carbonyl carbon is at 172.92 ppm; the peaks belonging to the carbon atoms in the pyridinium ring at the end are at 145.91, 145.17, 145.11, 140.42 and 136.15 ppm; the peaks belonging to the carbon atoms in the pyridinium ring connected to the amide functional group are at 147.39, 144.47, 142.46, 128.49 and 119.64 ppm. Apart from these, other characteristic carbon atoms, such as the peak of CH_2 carbon bonded to the pyridinium nitrogen at the end at 61.02 ppm; the peak of CH_2 carbon bonded to the pyridinium nitrogen attached to the amide functional group at 53.41 ppm; the peak of CH_2 carbon adjacent to the carbonyl group at 46.02 ppm and the peak of CH_3 carbon at the very end of the long chain at 14.35 ppm.

Table 1. The characterization results of the synthesized surfactant.

Compound	Characterization data
DPUP (3)	FT-IR (ATR, $\tilde{\nu}$/cm^{-1}): 3300 (amide, N–H), 3088 (aromatic C–H), 3061 (aromatic C–H), 2924 and 2854 (aliphatic C–H), 1662 (amide C=O), 1432 (amide C–N). ^{1}H NMR (600 MHz, DMSO-d6): δ (ppm) = 10.52 (1H, amide, N–H), 9.19, 8.14, 7.94, 7.76 (4H, aromatic C–H, O=C–NH–Py–H), 9.02, 7.99, 7.83 (5H, aromatic C–H, –CH$_2$–CH$_2$–Py–H), 4.63 (2H, CH$_2$, O=C–NH–PyN$^+$–CH$_2$), 4.17 (2H, CH$_2$, PyN$^+$–CH$_2$–CH$_2$), 2.47 (2H, CH$_2$, –CH$_2$–CH$_2$–(C=O)–NH), 2.34 (2H, CH$_2$, –CH$_2$–CH$_3$), 1.86 (2H, CH$_2$, O=C–NH–PyN$^+$–CH$_2$–CH$_2$), 1.61 (2H, CH$_2$, CH$_2$–CH$_2$–C=O), 0.77 (3H, CH$_3$). ^{13}C NMR (150 MHz, DMSO-d6): δ (ppm) = 172.92 (1C, C=O), 147.39, 144.47, 142.46, 128.49, 119.64 (5C, O=C–NH–Py–C), 145.91, 145.17, 145.11, 140.42, 136.15 (5C, –CH$_2$–CH$_2$–Py–C), 61.02 (1C, PyN$^+$–CH$_2$–CH$_2$), 53.41 (1C, O=C–NH–PyN$^+$–CH$_2$), 46.02 (1C, –CH$_2$–CH$_2$–(C=O)–NH), 14.35 (1C, –CH$_2$–CH$_3$). Anal. Calcd. for C$_{33}$H$_{55}$Br$_2$N$_3$O (MW = 669.62 g/mol): C, 59.19; H, 8.28; N, 6.28. Found: C, 59.32; H, 8.40; N, 6.15.

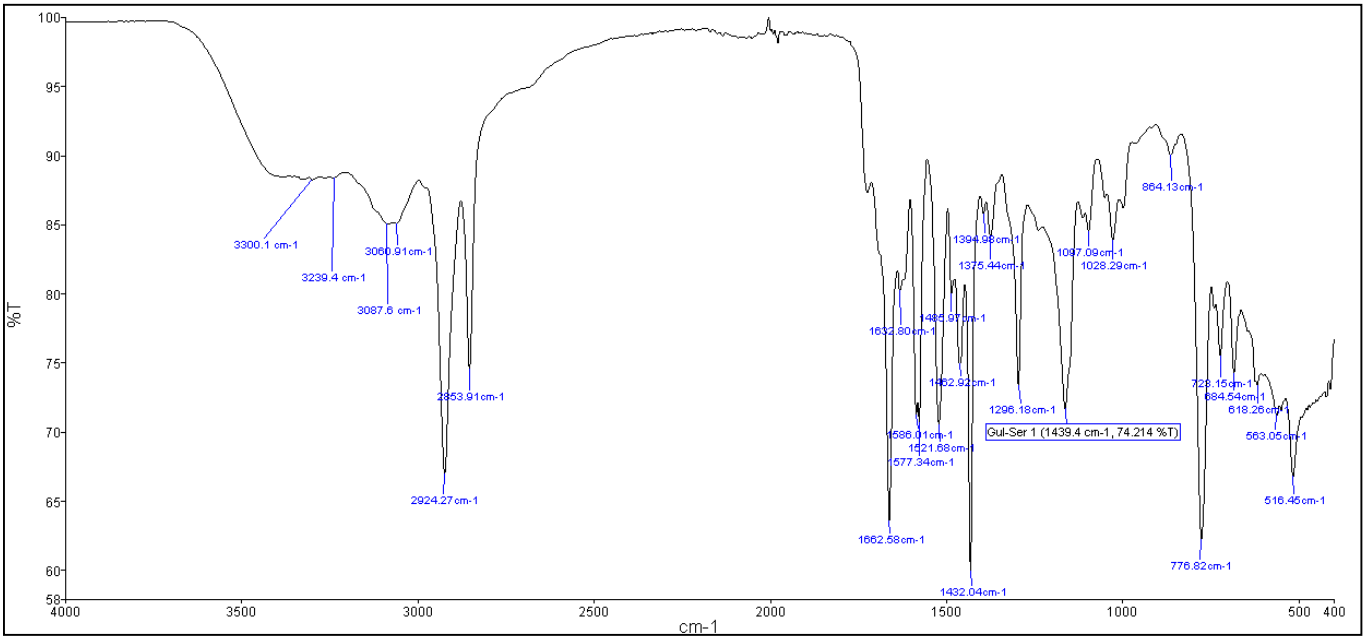

Figure 1. FT-IR spectrum of DPUP (3).

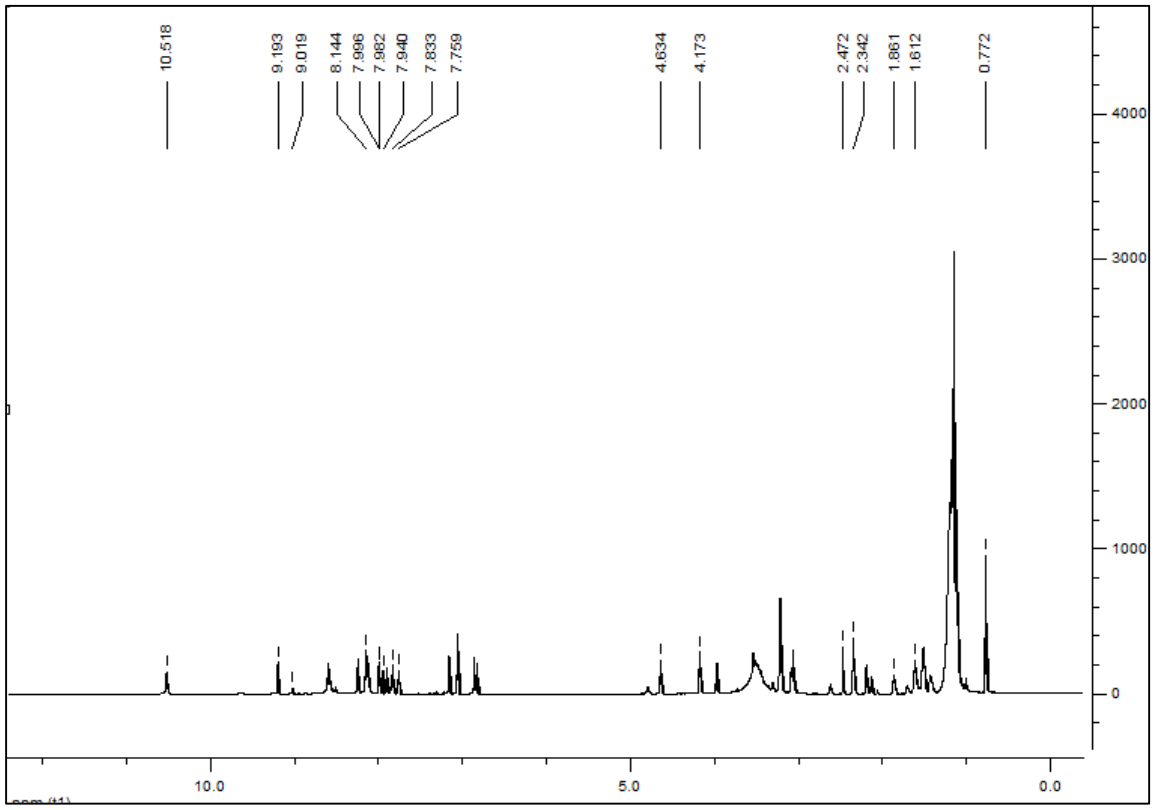

Figure 2. ^{1}H NMR spectrum of DPUP (3).

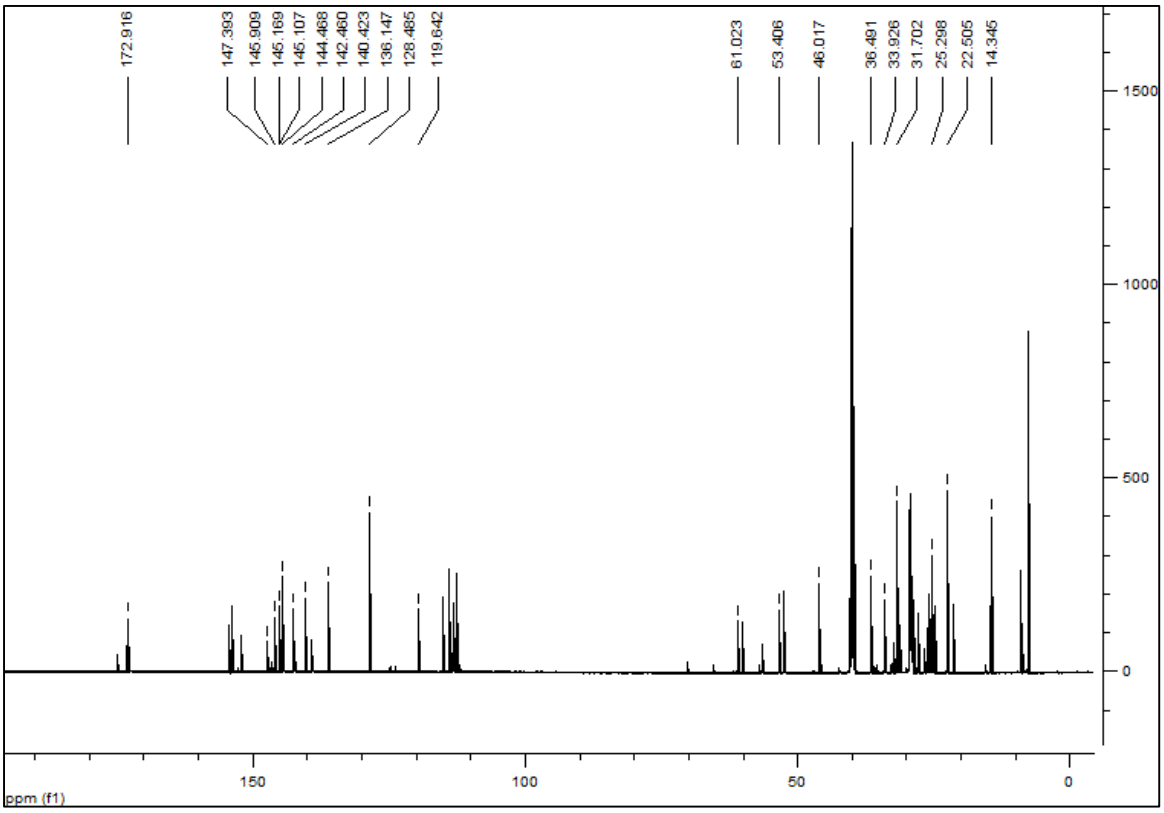

Figure 3. ^{13}C NMR spectrum of DPUP (3).

3.2. Anti-corrosion performance of DPUP (3)

3.2.1. Open circuit potential

In this study, OCP measurements were performed to determine the passivation properties acquired by the metal surface in a corrosive environment through the use of inhibitors. The obtained OCP data were evaluated to observe potential shifts caused by the use of inhibitors and to examine the passivation process on the metal surface. The measurements revealed how the potential changed over time, depending on the inhibitor concentrations, and demonstrated the effectiveness of inhibitors in slowing down the corrosion rate.

Figure 4 illustrates the changes in OCP over time under four different conditions (without inhibitor and with inhibitor concentrations of 2 ppm, 10 ppm, and 50 ppm). The OCP was measured with respect to the SCE and is expressed in voltage. Negative voltage values indicate the resistance of the tested material to corrosion. A more negative OCP value is generally associated with a higher corrosion rate.

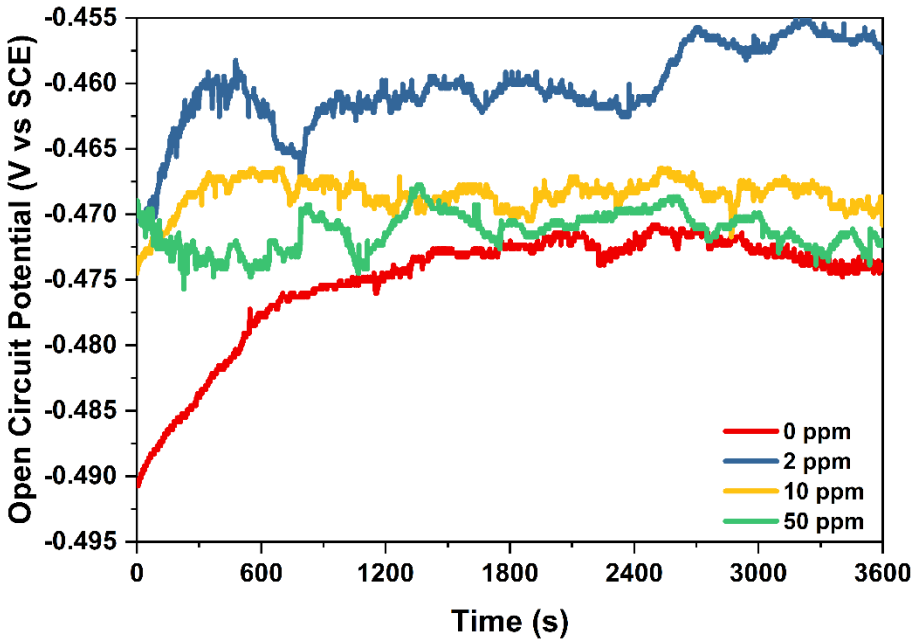

Figure 4. E_{OCP} *versus* time curves for mild steel in 1.0 M HCl solution at 25°C in the absence and in the presence of different concentrations of DPUP (3).

The black line in the graph represents the measurements conducted without an inhibitor, and as observed, this potential is quite negative. This negative potential suggests that the metal rapidly begins to oxidize in the natural corrosion process and that the surface is quickly deteriorating in the corrosive environment. With the addition of the inhibitor (at 2, 10 and 50 ppm), a significant positive shift in the OCP curves is observed. Particularly at 50 ppm concentration, the potential reaches a more positive and stable value. This positive shift indicates that inhibitor molecules have adsorbed onto the metal surface, limiting the electrochemical interactions between the metal surface and the environment. Inhibitor

molecules form a barrier between the metal surface and corrosive ions, thereby slowing down the corrosion process. The positive shift in OCP values becomes more pronounced with increasing inhibitor concentration, confirming that inhibitors provide stronger protection for the metal surface. Specifically, at 50 ppm concentration, it is clear that the potential shows a more stable trend, and the corrosion process has significantly slowed down.

3.2.2. Electrochemical impedance spectroscopy

Following the determination of OCP measurements, electrochemical impedance measurements were conducted. This method was chosen because it does not damage the adjusted 1.0 cm^2 surface area. In contrast, the Tafel extrapolation method leads to corrosion, which damages the metal surface.

Electrochemical impedance spectroscopy (EIS) data were analyzed using the Randles equivalent circuit, which includes the solution's ohmic resistance (R_s), charge transfer resistance (R_{ct}), and the Constant Phase Element (CPE; Q, α) that describes the non-ideal capacitive behavior at the interface. The CPE element models deviations from the ideal behavior of a classical capacitor due to surface roughness, heterogeneity, and distributed time constants. The impedance of this element is expressed by the following equation:

$$Z_{\mathrm{CPE}} = \frac{1}{Q(j\omega)^{\alpha}},\ 0 < \alpha \leq 1 \tag{9}$$

Here, the constant Q represents the system's capacitance magnitude, while the parameter α represents the degree of surface homogeneity. As the α value approaches 1, the system approaches ideal capacitive behavior. The total impedance of the circuit is defined as follows:

$$Z(\omega) = R_s + \left[\frac{1}{R_{ct}} + Q(j\omega)^{\alpha}\right]^{-1} \tag{10}$$

Experimental data were fitted to this model using the complex least squares method, with fitting performed on both the real and imaginary components. The double-layer capacitance (C_{dl}) was calculated using the Hsu–Mansfeld approach when the CPE was in parallel with R_{ct}:

$$C_{dl} = (QR_{ct}^{1-\alpha})^{1/\alpha} \tag{11}$$

The CPE-equipped Randles circuit (R_s–(R_{ct}‖CPE)) is shown in Figure 5.

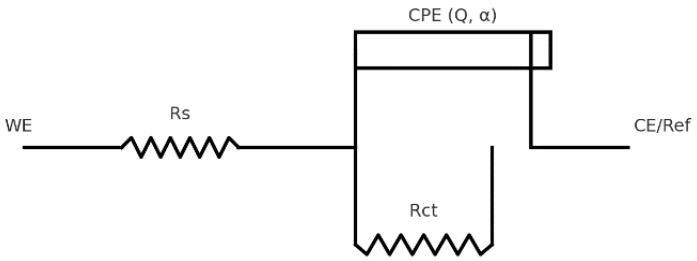

Figure 5. CPE-equipped Randles circuit (R_s–(R_{ct}‖CPE).

Figure 6 shows the Nyquist diagram. The Nyquist diagram shown in Figure 6 displays a single suppressed semicircle for all concentrations, indicating that the system exhibits load transfer controlled behavior. The absence of any 45° Warburg tail in the low frequency region confirms that ion transport is not a limiting step. The points intersecting the Z' axis at high frequency represent the ohmic resistance (R_s) of the solution. The R_s values (5.51–30.30 Ω) remained quite small compared to R_{ct}, indicating that the addition of the inhibitor did not significantly affect the conductivity of the solution.

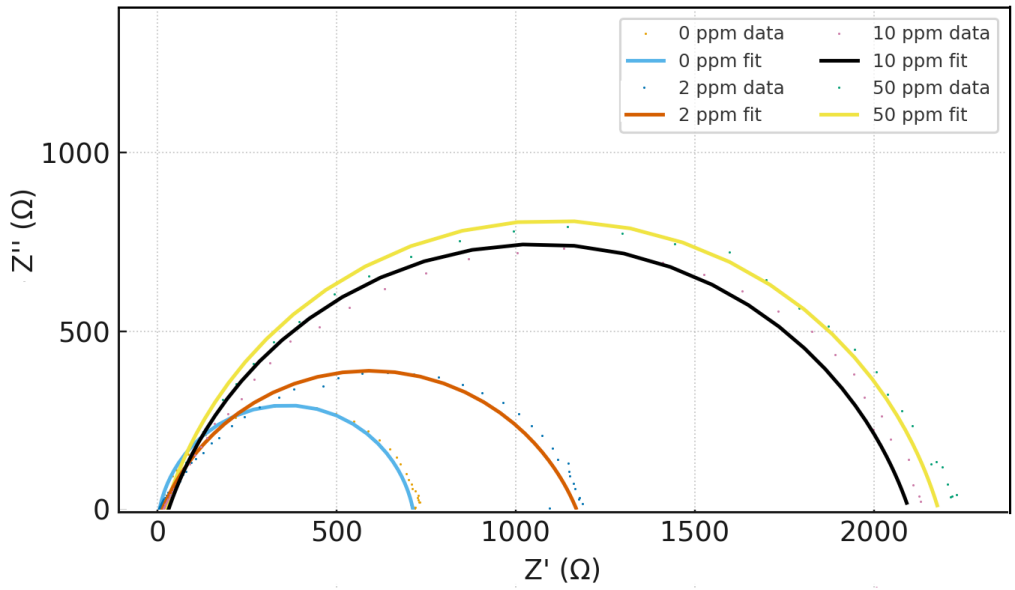

Figure 6. Electrochemical impedance spectrum according to Nyquist format for mild steel at 25°C in 1.0 M HCl solution without DPUP (3) and with various concentrations of DPUP.

The effect of inhibitor usage is clearly observed in the Nyquist diagram through the increasing size of the semicircles. As the inhibitor concentration increases (2 ppm, 10 ppm, 50 ppm), the diameter of the semicircle also grows. As shown in the EIS parameters presented in Table 2, the increase in half-circle diameters along with the inhibitor concentration caused the load transfer resistance (R_{ct}) to rise from 708.7 Ω to 2159.7 Ω. This increase indicates that inhibitor molecules adsorb onto the surface, reducing the active area at the metal–solution interface and thus hindering electron transfer, thereby decreasing the

corrosion rate. The 50 ppm concentration, at which the widest semicircle was observed, indicates that the surface is almost completely covered by an inhibitor layer and that maximum protection efficiency is achieved. The inhibitor molecules adsorbed onto the metal surface prevent corrosive ions from reaching the metal, thereby slowing down the corrosion process.

The CPE exponent value ($\alpha<1$) explains the flattened appearance of the semicircles and indicates the rough and heterogeneous structure of the surface. The CPE parameter (Q) and the derived double-layer capacitance (C_{dl}) values showed a slight increase at low concentrations and a decreasing trend at high concentrations. This situation indicates that the inhibitor forms a more compact and homogeneous film layer on the surface with increasing concentration, reducing the active areas by limiting ion passage. As a result, it is understood that the system is successfully defined by the R_s–(R_{ct}‖CPE) model and that corrosion resistance increases significantly with increasing inhibitor concentration.

Table 2 shows an increase in R_s values with inhibitor concentration is also observed, indicating that the resistance of the electrolyte solution has increased due to the inhibitor's effect. Table 2 also includes the inhibitor efficiency (η_{EIS}), which measures the inhibitor's effectiveness in preventing metal surface corrosion. The η_{EIS} values for DPUP (3) in Table 2 were derived using Equation (12) [22]. This equation quantitatively shows the extent to which the protective layer formed by the inhibitor on the surface inhibits charge transfer. At a concentration of 2 ppm, the efficiency is 38.82%, but it increases to 67.19% at 50 ppm. This indicates that higher inhibitor concentrations significantly enhance corrosion prevention efficiency.

$$\eta_{EIS}(\%) = \left(\frac{R_{ct(inh)} - R_{ct(blank)}}{R_{ct(inh)}} \right) \cdot 100 \qquad (12)$$

Table 2. EIS parameters for mild steel in 1.0 M HCl solution in the absence and presence of the different concentration of DPUP (3) at 25°C.

Concentration	R_s **(Ω)**	C_{dl} **(μF)**	R_{ct} **(Ω)**	Q **(F·s$^{\alpha-1}$)**	**α (CPE exponent)**	η_{EIS} **(%)**
Without inhibitor	5.51	2.55	708.67	4.09×10^{-5}	0.88	–
2 ppm	13.03	1.74	1158.41	4.52×10^{-5}	0.76	35.5
10 ppm	30.30	2.61	2068.78	4.76×10^{-5}	0.79	66.1
50 ppm	21.47	1.69	2159.68	3.07×10^{-5}	0.82	96.4

3.2.3. Tafel polarization curves

Figure 7 shows the Tafel curves. In the case without the inhibitor (black line), it can be observed that the corrosion current is quite high, and the potential values are more negative. This indicates that the metal quickly engages in the corrosion process and deteriorates

rapidly in the corrosive environment. With the use of inhibitors (2 ppm, 10 ppm, 50 ppm), a significant decrease in the corrosion current is observed, along with more positive potential values in the Tafel curves. At an inhibitor concentration of 50 ppm, the corrosion current (i_{corr}) reaches its lowest level ($1.96 \cdot 10^{-6}$ A/cm^2), indicating that the inhibitor effectively adsorbs onto the metal surface and significantly slows the corrosion process.

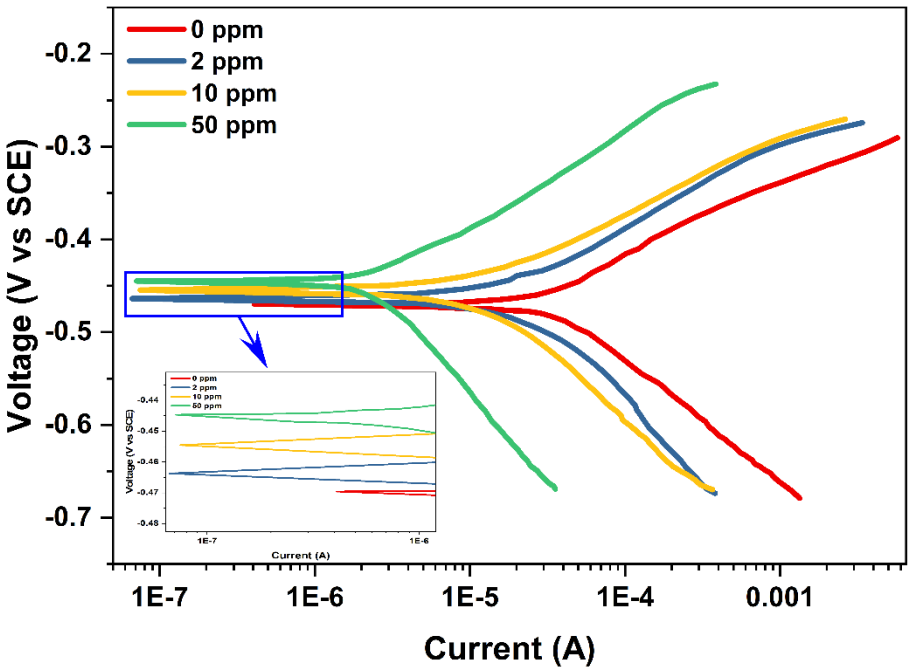

Figure 7. Potentiodynamic polarization curves obtained for mild steel in 1.0 M HCl solution devoid and containing various concentrations of DPUP (3) at 25°C.

The corrosion parameters presented in Table 3 confirm these observations. In the absence of the inhibitor, the corrosion rate (*CR*) is quite high (0.0515 μm/year); however, with the use of the inhibitor, this value decreases significantly. Specifically, at a 50 ppm inhibitor concentration, the corrosion rate drops to 0.0035 μm/year. This result clearly shows that the inhibitor greatly reduces the corrosion rate by forming a protective layer on the metal surface. The corrosion potential (E_{corr}) also shifts to more positive values with increasing inhibitor concentration, confirming that the metal surface becomes passivated and the corrosion process slows down.

Looking at how inhibitor concentration changes corrosion inhibition efficiencies, at 2 ppm concentration the inhibitor efficiency was 32.3%, while at 50 ppm concentration this value increased up to 93.3%. Based on the data presented in Table 3, the corrosion test results for inhibitor DPUP (3) at varying concentrations indicate that as the concentration increases, the corrosion rate decreases while the percentage inhibition efficiency improves. This trend is attributed to the increased amount of material adhering to the surface with higher concentrations [23–25]. The values for inhibition efficiency (η_{PDP}) and CR presented in Table 3 were derived using Equations (13) and (14), as referenced in [26, 27].

$$\eta_{PDP} = \frac{i_0 - i_{corr}}{i_0} \cdot 100 \quad (13)$$

where i_0 represents the corrosion current density of the samples without the film, and i_{corr} denotes the corrosion current density of the samples with the film.

$$CR = \frac{i_{corr} M}{FzD} \quad (14)$$

where M is the molecular weight, F is the Faraday's constant, z is the metal's valence and D is the density of the metal.

Table 3. Tafel polarization parameters for mild steel in 1.0 M HCl solution in the absence and presence of the different concentration of DPUP (3) at 25°C.

Concentration	E_{corr} **(V)**	i_{corr} **(A/cm^2)**	**CR (μm/year)**	η_{PDP} **(%)**
Without inhibitor	–0.465	2.91×10^{-5}	0.0515	–
2 ppm	–0.459	1.97×10^{-5}	0.0348	32.3
10 ppm	–0.457	1.02×10^{-5}	0.0180	65.0
50 ppm	–0.465	1.96×10^{-6}	0.0035	93.3

The inhibitor's presence in the acid solution influences both the anodic and cathodic branches. This dual effect suggests that the inhibitor provides mixed-type corrosion inhibition. From Figure 4, we can see that the corrosion potential (E_{corr}) curves are slightly shifted in both positive and negative directions in the presence of the prepared surfactants, indicating that the synthesized surfactant is a mixed type inhibitor [28, 29]. The mixed inhibitory behavior can be described as follows: In a blank acid solution, anions like Cl^- ions are drawn to the anode (positive), while cations such as H^+ ions are attracted to the cathode (negative) [30]. Consequently, oxidation-reduction reactions occur complementarily. The synthesized di-cationic surfactant contains Br^- and pyridinium cationic (N^+) groups. Therefore, in an HCl solution with the inhibitor, Br^- competes with Cl^- for adsorption at the anode, and N^+ competes at the cathode. Br^- is more likely to adsorb than Cl^- due to its larger atomic radius and lower electronegativity [30]. This results in better Br^- adsorption at the anode, facilitating increased DPUP (3) adsorption through coulombic electrostatic attraction. The structure of DPUP (3) also contains an O atom containing an electron pair and two pyridinium rings containing pi-electrons. The compound can donate these electron pairs to the *d*-orbital of Fe [31]. Due to the greater adsorption ability of the bromide ion and the donor-acceptor interactions in the anodic region where the corrosion event takes place, it produces a strong corrosion inhibitory effect.

3.3. Adsorption isoterm

The corrosion inhibition mechanism can be understood by studying how molecules bind to the metal surface's active sites. Adsorption isotherm experiments reveal the nature of this molecular binding. Organic inhibitors prevent corrosion by displacing water molecules that are attached to the metal surface. This is the accepted view of how they work. There are two modes of adsorption for organic inhibitor molecules on a metal surface. The two types of adsorption are electrostatic and chemical. The former involves physical attraction, while the latter involves chemical bonding [32–34]. The Langmuir isotherm showed the best fit among the different standard adsorption isotherms. This is because the Langmuir isotherm plots had the highest linear correlation coefficient ($R^2 = 1$). These graph is shown in Figure 8. As the Langmuir model fits the data, the adsorption of cationic surfactant on the low carbon steel surface in 1.0 M HCl solution is likely a monolayer adsorption [35]. The Langmuir adsorption isotherm is characterized by equation 15 [36].

$$\frac{C_{\text{inh}}}{\theta} = \frac{1}{K_{\text{ads}}} + C_{\text{inh}} \tag{15}$$

The weight loss values obtained are used to calculate the surface coverage (θ), which is the fraction of the surface occupied by the inhibitor molecules in M. The adsorption-desorption equilibrium constant (K_{ads}) and the inhibitor concentration (C_{inh}) are related to the surface coverage by equation 16 [37].

$$\theta = \left(\frac{W_0 - W}{W_0} \right) \tag{16}$$

W_0 is the weight loss of metal in corrosive solution without inhibitor, W is the weight loss of metal in corrosive solution with inhibitor. Figure 8 shows the plots of C_{inh} *versus* C_{inh}/θ. The K_{ads} values of cationic surfactant for different immersion times were calculated from the intersection of the linear graph in Figure 8, and these values are given in Table 4. As seen in Table 4, K_{ads} values were determined as $27.24 \cdot 10^5$ M^{-1} for 6 hours immersion time, $104.28 \cdot 10^5$ M^{-1} for 24 hours immersion time, $258.59 \cdot 10^5$ M^{-1} for 48 hours immersion time and $202.70 \cdot 10^5$ M^{-1} for 72 hours immersion time. Except for 72 hours of immersion time, we can generally say that K_{ads} values increased as the immersion time increased. That is, the ability of the surfactant to adsorb on the metal surface increased as the immersion time increased. From the K_{ads} values, it can be concluded that the strongest bond between the inhibitor molecule and the metal surface should be at 48 hours immersion time [19]. To clarify this point, the Gibbs free energy values (ΔG^0_{ads}) of adsorption of cationic surfactant for different immersion times were calculated as shown in equation 17 below [38].

$$\Delta G^0_{\text{ads}} = -RT \ln(55.5 K_{\text{ads}}) \tag{17}$$

where R is the universal gas constant, T is the absolute temperature and 55.5 is the molar concentration of water in solution. The ΔG^0_{ads} values for different immersion times are shown in Table 4. Negative Gibbs free energy values indicate that the adsorption of the surfactant to the metal surface occurs spontaneously at each immersion time. However, in a general approach, electrostatic interactions between charged molecules and the charged metal (physical adsorption) are effective at Gibbs free energy values up to –20 kJ·mol^{-1}, while chemical adsorption involving electron sharing or transfer from inhibitor molecules to the metal surface is more effective at values more negative than –40 kJ·mol^{-1} [37]. Looking at the ΔG^0_{ads} values calculated for 6, 24, 48, and 72 hours immersion times in Table 4, it is possible to say that chemical adsorption is more effective in the adsorption of the inhibitor on the metal surface. In the adsorption mechanism shown in Figure 9, it is displayed how the di-cationic surfactant used as an inhibitor is attached to the metal surface by chemical and physical adsorption. When the structure of the synthesized di-cationic surfactant is examined, it is seen that there are two pyridinium rings as cationic groups. As seen in Figure 9, the metal surface, which was positively charged as a result of the oxidation of iron to the +2 oxidation step in the anode reaction, turned negative by forming a dipole under the influence of chloride ions from the acid and bromide ions from the compound [23, 39]. The negatively charged dipole and the positively charged nitrogen atoms of the inhibitors interact via electrostatic interaction (physical adsorption) and adsorb to the metal surface. In addition, the unpaired electron pairs in the oxygen atom and π-electrons in the aromatic pyridinium ring in the structure of the compound interact with the empty d orbitals of the Fe element in the metal plates and attach to the metal surface by chemical adsorption. As a result of both chemical and physical adsorption, the negative effect of acidic corrosive environment on the metal surface is prevented.

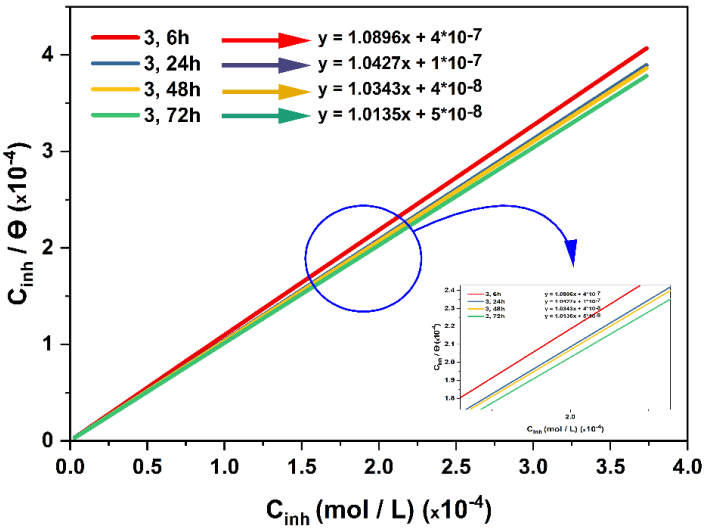

Figure 8. Langmuir adsorption plots obtained from mass loss values for carbon steel exposed to different immersion times in 1.0 M HCl in the presence of different concentrations of the di-cationic surfactant.

Table 4. Adsorption equilibrium constants (K_{ads}) and Gibbs free energy values (ΔG^0_{ads}) of DPUP(3) determined according to Langmuir isotherm.

Surfactant	**K_{ads} ($\times 10^5$ M^{-1})**				**ΔG^0_{ads} (kJ mol^{-1})**			
DPUP (3)	6h	24h	48h	72h	6h	24h	48h	72h
	27.24	104.28	258.59	202.70	–46.66	–49.99	–52.24	–51.64

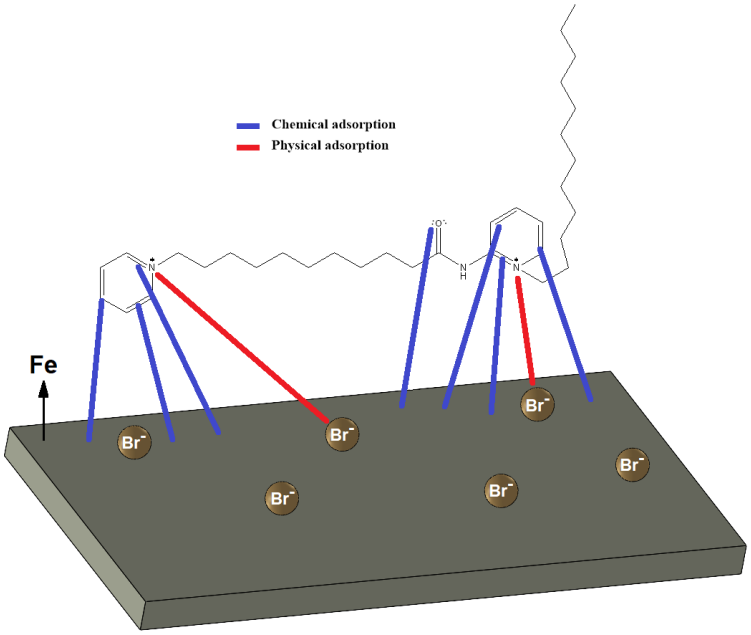

Figure 9. Adsorption mechanism of DPUP (3) on the metal surface.

3.4. SEM and EDX analyses

The SEM images in Figure 10 illustrate the detailed changes in the metal surface before and after exposure to a 1.0 M HCl solution, both with and without the inhibitor. These images highlight the morphological differences of the metal surface, enabling a visual assessment of the inhibitor's effectiveness against corrosion. The initial SEM image (Figure 10a) depicts the metal surface prior to immersion in a 1.0 M HCl solution. The surface appears relatively smooth and linear, with no significant signs of deformation or corrosion, aside from minor scratches and fine roughness. This suggests that the metal surface is clean and smooth, representing a pristine state where corrosion has not yet begun. On a microscopic level, the metal surface shows minimal deterioration and no evident traces of corrosion. The second SEM image (Figure 10b) illustrates the metal surface after 24 hours of immersion in a 1.0 M HCl solution without an inhibitor. The image reveals extensive corrosion products on the metal surface, which is now severely pitted and distorted. Corrosion has significantly impacted the metal, resulting in a highly irregular surface. The observed roughness and corrosion products indicate rapid corrosion in the HCl environment, leading to substantial

surface deformation. The metal surface is notably damaged and exhibits a non-homogeneous morphology. This image clearly demonstrates the rapid corrosion of the metal in an acidic environment without inhibitors, resulting in severe surface deformation.

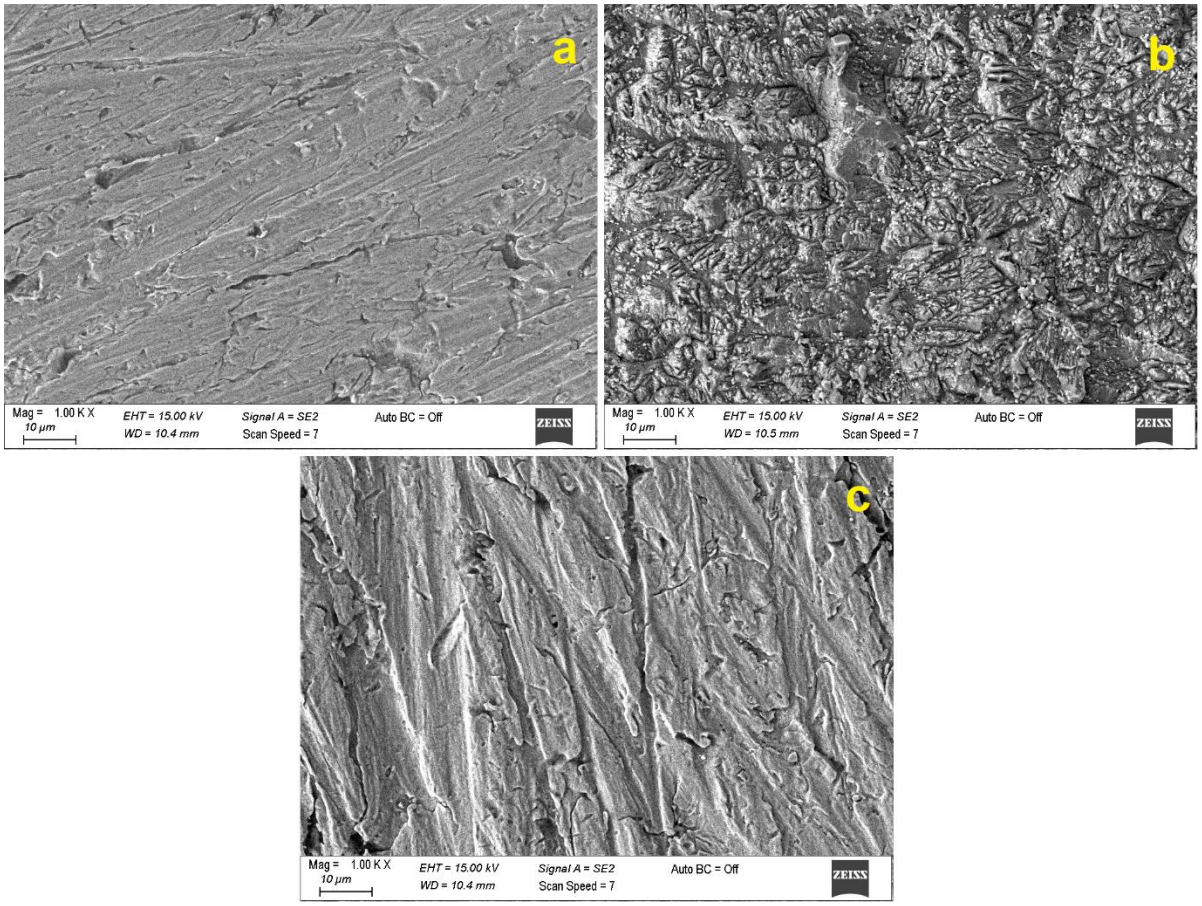

Figure 10. Scanning electron microscopy (SEM) images of the metal surface **a)** before immersion in the corrosive 1.0 M HCl solution, **b)** after 24 h of immersion in 1.0 M HCl without inhibitor, and **c)** after 24 h of immersion in 1.0 M HCl with 50 ppm inhibitor.

The third SEM image (Figure 10c) depicts the metal surface after 24 hours of immersion in a 1.0 M HCl solution containing 50 ppm of inhibitor. The metal surface remains relatively smooth with no significant signs of corrosion, thanks to the inhibitor. Although some fine lines from sanding are still visible, the inhibitor has largely protected the metal surface. By forming a protective layer, the inhibitor has significantly prevented surface degradation. The deformations on the surface are minimal compared to the severe corrosion observed without the inhibitor. This suggests that the inhibitor is effectively adsorbed onto the metal surface, inhibiting corrosion reactions. Consequently, the morphology of the metal surface was largely preserved, and irregular deterioration was minimized. At a concentration of 50 ppm, the inhibitor successfully protected the metal surface from the acidic environment, preventing serious deterioration.

Figure 11 presents the 3D surface topographies and height distributions generated from the SEM images in Figure 10 using the Gwyddion software. In this modeling, the x- and y-axis dimensions were obtained from the SEM images and defined in the software in micrometers (μm). The z-axis, on the other hand, was created by assigning grayscale values to the SEM images using Gwyddion, which normalized these values between 0 and 100 to provide depth and height information. This method allowed for the determination of surface profiles and comparison of height parameters. These analyses performed with Gwyddion software were conducted to facilitate understanding the morphological changes on the surfaces of metals under different conditions.

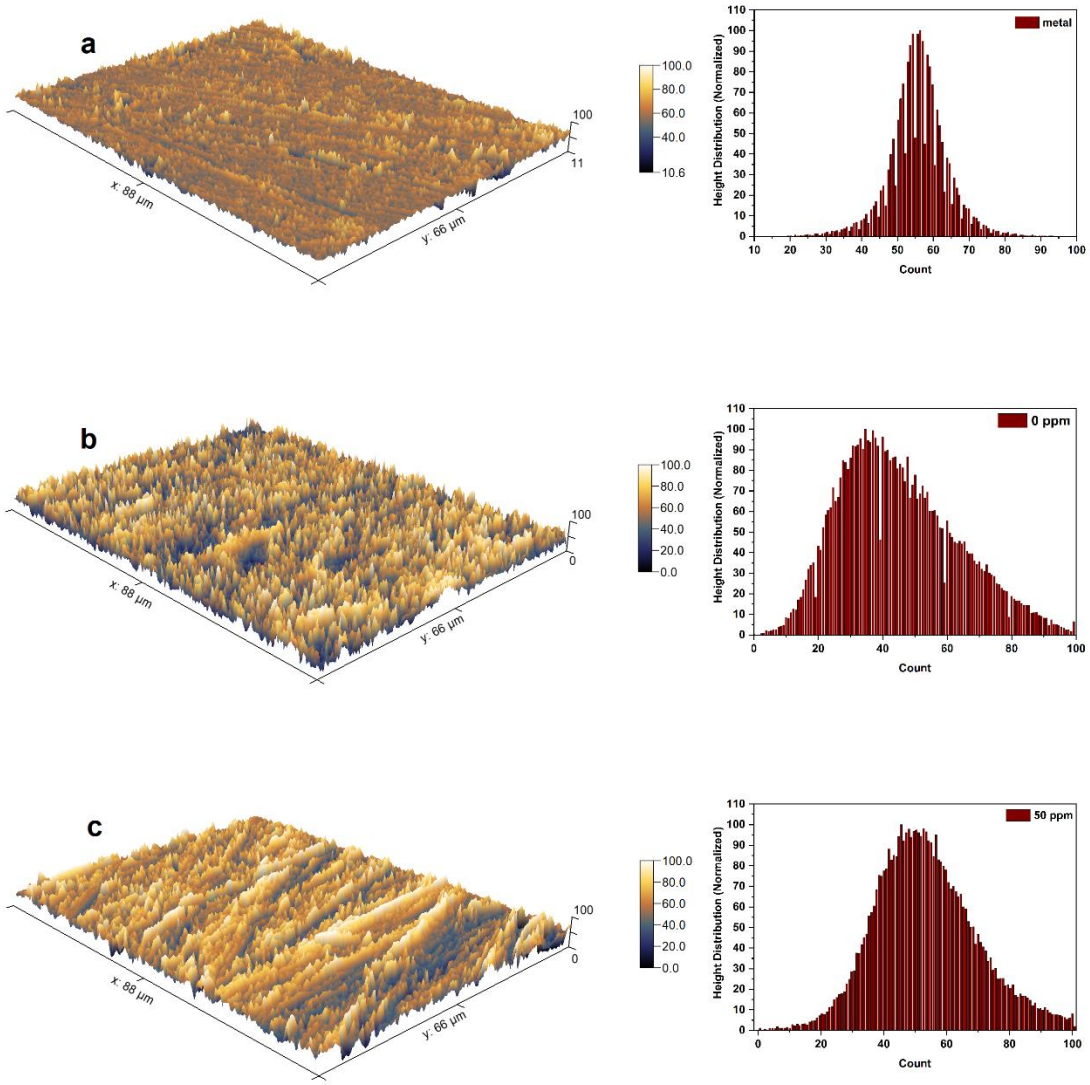

Figure 11. 3D surface modeling derived from SEM images.

The pristine metal surface, represented in image (a), exhibits a highly homogeneous topography with limited height variations. This indicates the smoothness of the metal surface and the absence of any corrosion effects. The histogram shows a narrow distribution, with roughness values concentrated around 50 units, confirming the initial homogeneous

morphology of the surface. In contrast, the metal surface exposed to an HCl environment without an inhibitor, as shown in image (b), displays a highly irregular topography with the formation of pits and peaks. The z-axis values range widely from 0 to 100, indicating severe pitting corrosion. The histogram demonstrates a broader distribution, with roughness values peaking around 70 units, confirming significant surface damage caused by corrosion. The metal surface exposed to an environment with 50 ppm inhibitor, as depicted in image (c), shows a considerable reduction in roughness, with the surface remaining relatively smooth. This indicates that the inhibitor effectively forms a protective layer on the surface, preventing corrosion. The histogram shows a narrow distribution, with height values concentrated around 60 units, further supporting the effectiveness of the inhibitor.

These findings collectively demonstrate that corrosion in the absence of an inhibitor causes severe damage to the surface, while the presence of 50 ppm inhibitor significantly preserves the original structure of the surface. These results confirm that inhibitors are an effective solution for protecting metal surfaces in acidic environments.

Figure 12 presents the Energy Dispersive X-Ray Spectroscopy (EDX) analysis, which investigates the chemical composition of elements on the metal surface. This analysis helps to understand the distribution of elements on the surface and the impact of inhibitors on corrosion. The EDX results illustrate the changes in the metal surface in a 1.0 M HCl solution under three conditions: before immersion, without an inhibitor, and with 50 ppm of inhibitor.

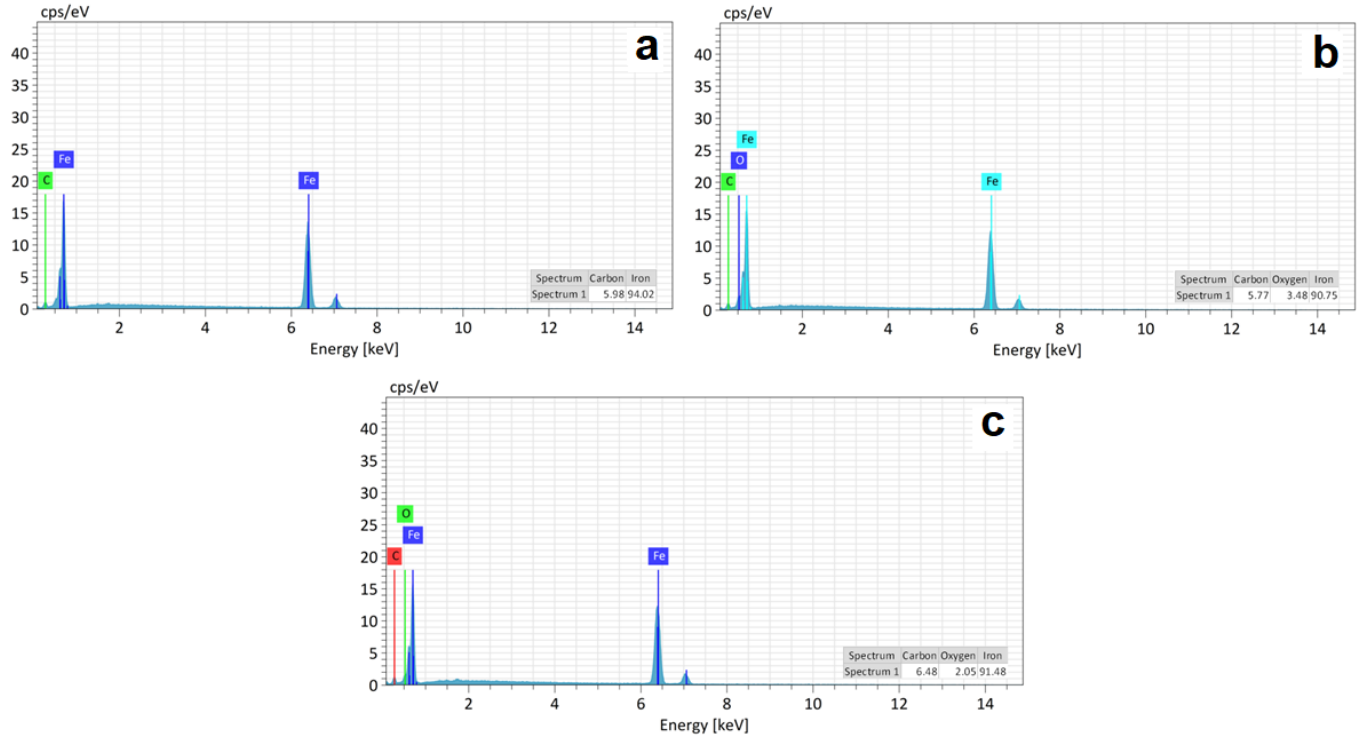

Figure 12. Energy dispersive X-ray spectroscopy (EDX) spectra obtained for the metal surface **a)** before immersion in corrosive 1.0 M HCl solution **b)** after 24 h of immersion in 1.0 M HCl without inhibitor, and **c)** after 24 h of immersion in 1.0 M HCl with 50 ppm inhibitor.

In the EDX spectrum prior to immersion (Figure 12a), iron (Fe) is the dominant element on the metal surface. Small quantities of carbon (C) are also detected, consistent with the use of low carbon steel. The prominent iron peak in the spectrum indicates the primary composition of the metal. This represents the pure metal surface before any protective layer has formed [40]. In the second scenario (without an inhibitor) (Figure 12b), a prominent oxygen peak is observed on the surface after 24 hours of exposure to the inhibitor-free solution. This peak signifies the onset of oxidation and the progression of corrosion on the metal surface. It is believed that Fe_2O_3 (iron (II) oxide) and other oxides, such as $Fe(OH)_3$ [41], have formed extensively on the metal surface. The presence of carbon and oxygen peaks indicates surface deterioration as corrosion advances. The oxygen peak, in particular, highlights the oxidation of iron. Although the iron peak is still present, it is relatively lower due to the oxidation process. The advancement of corrosion suggests that a significant portion of the iron on the surface has oxidized, leading to surface degradation [19].

In the third scenario (with 50 ppm inhibitor) (Figure 12c), the levels of oxygen and carbon are lower compared to the inhibitor-free environment. This suggests that the inhibitor effectively protects the metal surface, preventing oxygen from reacting electrochemically with iron. Consequently, the iron peak is higher in the presence of the 50 ppm inhibitor. This indicates that the inhibitor forms a protective layer on the metal surface, preventing corrosion. The reduced levels of oxygen and carbon confirm that the inhibitor adsorbs onto the surface, significantly inhibiting corrosion reactions. Thus, the inhibitor successfully protects the metal from corrosion [40].

3.6. Contact angle measurement

The contact angle measurements determined by the pure water drop method dropped on the metal surface are visually shown in Figure 13. The contact angle values measured based on these images are given in Table 5.

Table 5. Contact angle and total surface energy values determined for pure water dripped on the metal surface immersed in acid medium containing 50 ppm inhibitor and without inhibitor for 6 and 24 hours at 25ºC.

Contact angle (º)				**Total surface energy (mJ/m^2)**			
Without inhibitor		50 ppm DPUP		Without inhibitor		50 ppm DPUP	
6 hours	24 hours	6 hours	24 hours	6 hours	24 hours	6 hours	24 hours
68.91	40.35	79.11	77.57	67.3	113.0	51.5	53.8

Thermodynamically, atoms aim to minimize their surface area. In this context, surface tensions of liquids play a crucial role in wetting a surface. The primary forces involved are the cohesion forces between liquid molecules and the adhesion forces between the liquid and the surface. When cohesion forces are strong, liquids retain their drop shape on the surface,

resulting in larger contact angles. Conversely, if adhesion forces dominate, the liquid spreads across the surface, leading to smaller contact angles.

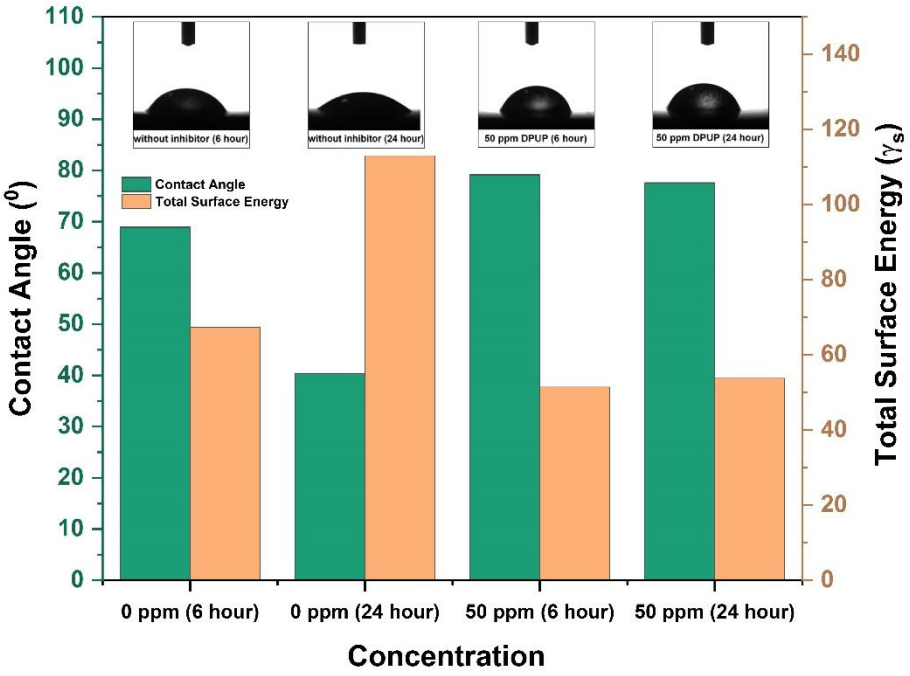

Figure 13. Contact angle images determined on metal surfaces removed from 1.0 M HCl solution without inhibitor and containing 50 ppm di-cationic surfactant.

In addition to the contact angle measurements, the total surface energy values were also analyzed. It was observed that higher total surface energy is associated with surfaces that exhibit smaller contact angles. For instance, in the case of the metal surface removed from the solution without the inhibitor, the total surface energy was higher due to the hydrophilic nature of the surface, which caused water to spread more. Conversely, the surfaces exposed to the inhibitor showed lower total surface energy values as a result of the hydrophobic layer formed by the di-cationic surfactant adsorbed on the metal surface.

Examining the contact angle values in Table 5, it was noted that the contact angle of pure water on the metal surface immersed in a 1.0 M HCl solution, both with and without inhibitors, decreased over a longer duration (24 hours). This outcome was anticipated. However, the contact angle on the metal surface removed from the acid containing the inhibitor was larger because the di-cationic surfactant adsorbed on the metal surface over time, rendering it hydrophobic. In contrast, the metal surface removed from the corrosive medium without the inhibitor remained hydrophilic, causing a water drop to spread more on the surface and reducing the contact angle. This difference in hydrophilicity is also reflected in the total surface energy values, where the metal surface exposed to the inhibitor showed significantly lower total surface energy compared to the untreated surface.

3.7. DFT calculations

The optimized molecule of DPUP (3) is shown in Figure 14. In general, the prediction of the inhibition behavior of electronic systems rests upon the capability to assess an important property, namely the global reactivity. Chemical reactivity can be understood in terms of the HOMO and the LUMO. E_{HOMO} is often associated with the electron donating ability of a molecule, whereas E_{LUMO} indicates the ability of a molecule to accept electrons. Therefore, a high value of E_{HOMO} and a low value of E_{LUMO} could suggest efficient adsorption process. Thus, lower is the energy gap (ΔE); better is the electron transfer process. Graphical representations of the frontier molecular orbitals HOMO and LUMO are shown in Figure 15. As is seen, the HOMO electron density of DPUP (3) is concentrated on the carbon atoms neighbouring the pyridine ring together with the Br atom, whereas the LUMO receives a relatively smaller contribution from those carbon atoms, and delocalizes onto the C and N atoms of pyridine ring.

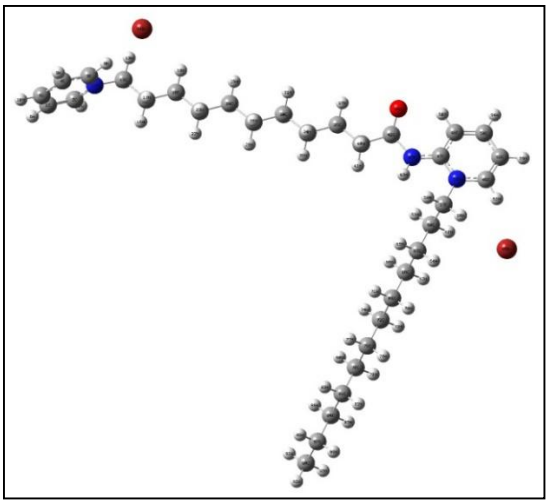

Figure 14. Optimized structure of DPUP (3) at the B3LYP/6-311++G(d,p) level.

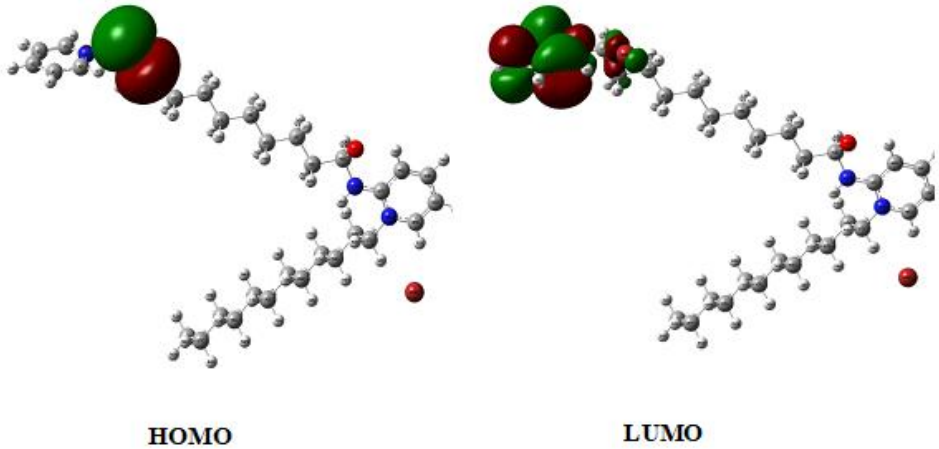

Figure 15. Visualization of the HOMO and LUMO iso-surfaces as derived at the B3LYP/6-311++G(d,p) level.

A molecule of high chemical hardness necessitates a significant energy input to undergo chemical alterations or interactions, attributed to a sizable energy barrier that hinders electron transfer. Conversely, a molecule denoted by substantial chemical softness, being the reciprocal of hardness, exhibits a marked propensity for electron transfer interactions. Switching to the assessment of nucleophilicity (ε) and electrophilicity (ω), which correspond to the capacity of an electron-rich molecule to donate electrons and an electron-deficient molecule to accept electrons, respectively. On the other hand, in the context of corrosion inhibition studies, the correlation between the fraction of electrons transferred (Δ*N*) and experimentally determined inhibition performance is of great importance (Table 6). One has to keep in mind, however, that Δ*N* values are not an unequivocal expression of the number of electrons transferred between the donor and acceptor species. A positive value of Δ*N* indicates that the transfer of electrons can take place, while a negative value indicates that the opposite is true. DPUP (3) exhibits a positive Δ*N* value, which implies a common propensity to facilitate electron transfer. The inhibitor does not exhibit a resistance to electron donation, suggesting that, in its interactions with other species, this compound is likely to participate in electron transfer reactions, which could influence its behavior in various chemical interactions. The electron-donating (ω^+) and electron-accepting (ω^-) power parameters for DPUP (3) further substantiate the findings from the Δ*N* value, reinforcing the notion of the molecule's readiness to participate in electron transfer interactions.

Table 6. Molecular electronic parameters.

Parameters	**DPUP (3)**
E_{HOMO} (eV)	–5.157
E_{LUMO} (eV)	–3.217
ΔE (E_L–E_H) (eV)	1.940
ω (eV)	9.037
χ (eV)	4.187
η (eV)	0.970
σ (eV^{-1})	0.515
ε (eV^{-1})	0.111
ω^+ (eV)	11.251
ω^- (eV)	7.064
Δ*N*	0.326

4. Conclusions

The conclusions of this study can be summarized as follows:

1) A di-cationic surfactant with two pyridinium rings was synthesized to combat the general corrosion of mild steel in a 1.0 M HCl acidic medium. Its structure was determined using spectroscopic techniques, including FT-IR and NMR.
2) The corrosion inhibition activities were examined using electrochemical techniques such as OCP, Tafel extrapolation, and EIS, which provide more precise and accurate results compared to the weight loss method. The inhibition efficiency at various concentrations was assessed and compared across different electrochemical methods. The results from both the potentiodynamic polarization and electrochemical impedance spectroscopy methods for the same inhibitor concentrations were found to be consistent and closely aligned.
3) As the concentration of the inhibitor increased, the corrosion rate on the metal surface decreased, leading to an enhanced corrosion inhibition efficiency of the di-cationic surfactant. This was evident from the decrease in corrosion current densities (i_{corr}) and the increase in corrosion resistance (R_{ct}) with higher inhibitor concentrations.
4) The effectiveness of the synthesized DPUP (3) compound in preventing metal corrosion is undeniably linked to its adsorption on the metal surface. One of the most effective ways to demonstrate that the di-cationic surfactant acts as a corrosion inhibitor by adsorbing onto the metal surface is by measuring the contact angle of pure water on the metal. The contact angle values observed on the metal surface immersed in a 1.0 M HCl solution with 50 ppm of the inhibitor for 6 and 24 hours were higher than those on the metal surface without the inhibitor. This indicates that DPUP (3) was adsorbed onto the metal surface, rendering it hydrophobic.
5) After confirming that the inhibitor adheres to the metal surface through contact angle measurements, the next question was to determine whether the adsorption was primarily physical or chemical. To address this, an adsorption isotherm study was conducted, revealing that the inhibitor follows the Langmuir adsorption isotherm. The K_{ads} and ΔG_{ads} values derived from this isotherm indicated a high adsorption capacity, suggesting that the inhibitor predominantly attaches to the metal surface through chemical adsorption.
6) SEM images were captured to visually demonstrate that the metal surface does not oxidize significantly and that the formation of corrosion products is weak in a 1.0 M HCl solution when the inhibitor is present. In the absence of the inhibitor, the accumulation of corrosion products on the metal surface was observed. In contrast, with the inhibitor present, the metal surface was much less affected by corrosion and exhibited a smoother appearance. This visual evidence confirmed that DPUP adsorbs onto the metal surface, protecting it from corrosion damage. This conclusion was further supported by changes in the elemental composition percentages on the surface, as revealed by EDX analysis. Additionally, 3D surface topographies generated using Gwyddion software further reinforced this conclusion. The pristine metal surface, modeled in Figure 11a, exhibited a

smooth and homogeneous morphology with minimal height variations, which was confirmed by a narrow roughness distribution. The metal surface exposed to the 1.0 M HCl solution without the inhibitor (Figure 11b) showed severe surface degradation, with significant peaks and valleys in the 3D model, reflecting the effects of intense pitting corrosion. The corresponding roughness distribution exhibited a broader range and higher roughness values, confirming the extensive damage. In contrast, the metal surface modeled in the presence of the inhibitor (Figure 11c) displayed a much smoother profile, with reduced height variations and a narrower roughness distribution. This indicates that the inhibitor formed a protective layer on the surface, effectively mitigating corrosion and preserving surface integrity.

7) By examining the factors that contributed to the understanding of corrosion inhibition through the DFT approach, it is evident that the calculated quantum chemical descriptors effectively elucidate the inhibition efficiency of DPUP (3). The analysis of HOMO and LUMO orbitals provided critical insights into the electronic properties of the inhibitor, highlighting its strong electron-donating (E_{HOMO}) and electron-accepting (E_{LUMO}) capabilities, as well as the significance of a low energy gap (ΔE). The HOMO electron density localized on the carbon atoms adjacent to the pyridine ring and the bromine atom indicates favorable sites for adsorption, while the LUMO's delocalization over the pyridine ring emphasizes its potential to interact with electron-donating surfaces. The parameters of chemical hardness and softness further substantiated the compound's high reactivity, with its chemical softness suggesting a strong propensity for electron transfer interactions. The positive ΔN value confirmed the ability of the inhibitor to donate electrons, corroborated by the ω^+ and ω^- parameters, which reinforce its readiness to engage in electron donation and acceptance processes. These findings collectively affirm that DPUP (3) participates actively in electron transfer interactions, which are pivotal to its corrosion inhibition mechanism.

Acknowledgements

We would like to thank Dr. Zafer Gültekin for his support in the electrochemical corrosion measurements in the experimental studies and for allowing us to use his handmade contact angle measuring device for contact angle measurements, which he has registered as a standard with patent application number 2024/009091.

We thank also the Bursa Uludag University Scientific Research Projects Association for their support under the project number FLO-2023-1452.

References

1. Shane, *Mild Steel Uses, Benefits, Properties, and Composition*, July 2nd, 2025. Link
2. J.K. Emmanuel, Corrosion protection of mild steel in corrosive media, a shift from synthetic to natural corrosion inhibitors: a review, *Bull. Natl. Res. Cent*., 2024, **48**, 26. doi: 10.1186/s42269-024-01181-7

3. J. Kaur, N. Daksh and A. Saxena, Corrosion inhibition applications of natural and eco-friendly corrosion inhibitors on steel in the acidic environment: An Overview, *Arabian J. Sci. Eng*., 2022, **47**, 57–74. doi: 10.1007/s13369-021-05699-0
4. S. Öztürk, Synthesis of 4-oxo-quinazoline derivative cationic surfactants showing inhibitor properties against the corrosion of low carbon steel in acidic medium, *Sakarya Univ. J. Sci.*, 2018, **22**, 986–1000. doi: 10.16984/saufenbilder.350569
5. B. El Ibrahimi, J.V. Nardeli and L. Guo, An overview of corrosion, *Sustainable Corrosion Inhibitors I: Fundamentals, Methodologies, and Industrial Applications*, ACS Symposium Series, American Chemical Society, Washington, DC, 2021.
6. A. Veeramanoharan and S.C. Kim, A comprehensive review on sustainable surfactants from CNSL: chemistry, key applications and research perspectives, *RSC Adv*., 2024, **14**, 25429–25471. doi: 10.1039/D4RA04684F
7. P. Madaan and V.K. Tyagi, Quarternary pyridinium salts: A review, *J. Oleo Sci*., 2008, **57**, 197–215. Link
8. S. Öztürk, G. Gece, A. Yıldırım and H. Gerengi, Newly synthesized pyridinium salt based tricationic surfactants as corrosion inhibitor for carbon steel in 1.0 M HCl medium, *Prot. Met. Phys. Chem. Surf*., 2023, **59**, 750–762. doi: 10.1134/S2070205123700673
9. G. Akgül and S. Öztürk, Synthesis of two cationic surfactants containing different functional groups linked to pyridinium nitrogen and their corrosion inhibition properties in 1.0 M HCl, *Ata-Kim. Derg*., 2023, **3**, 1–8.
10. R. Talat, M.A. Asghar, I. Tariq, Z. Akhter, F. Liaqat, I. Nadeem, A. Haider and S. Ali, Evaluating the corrosion inhibition efficiency of pyridinium-based cationic surfactants for EN3B mild steel in acidic-chloride media, *Coatings*, 2022, **12**, 1701. doi: 10.3390/coatings12111701
11. R. Ganjoo and A. Kumar, Current trends in anti-corrosion studies of surfactants on metals and alloys, *J. Bio. Tribo Corros*., 2022, **8**, 2. doi: 10.1007/s40735-021-00597-2
12. G. Gece, The use of quantum chemical methods in corrosion inhibitor studies, *Corros. Sci*., 2008, **50**, 2981–2992. doi: 10.1016/j.corsci.2008.08.043
13. A. Kokalj, Molecular modeling of organic corrosion inhibitors: Calculations, pitfalls, and conceptualization of molecule − surface bonding, *Corros. Sci*., 2021, **193**, 109650. doi: 10.1016/j.corsci.2021.109650
14. *Cold rolled low carbon steel flat products for cold forming – technical delivery conditions*, German version EN 10130:2006, DIN (Deutsches Institut für Normung e.V.) Standard, 2007.
15. S. Öztürk, Synthesis and corrosion inhibition behavior of novel amide-based quarternary di-cationic surfactants on carbon steel in HCl solutions, *Prot. Met. Phys. Chem. Surf*., 2018, **54**, 953–962. doi: 10.1134/S2070205118050167
16. S. Öztürk, Z. Gültekin, N.A. Gültekin, G. Akgül and M. Alper, Synthesis of di- and tricationic surfactants and comparison of their activity on oxidation of metal in HCl media, *Prot. Met. Phys. Chem. Surf*., 2023, **59**, 998–1009. doi: 10.1134/S2070205123700958

17. Z. Gültekin and N.A. Gültekin, Recycling a scrapped magnetic stirrer/heater using an arduino microcontroller, in: International Research in Science and Mathematics, Chapter 6, Serüven Publishing, Eds.: F. Özbaş Gerçeker, H. Akgül and H. Baba, ISBN: 978-625-6399-22-8, İzmir, Turkiye, 2022, p. 86.
18. S. Öztürk, A. Yıldırım, M. Çetin and M. Tavaslı, Synthesis of quaternary, long-chain N-alkyl amides and their corrosion inhibition in acidic media, *J. Surfactants Deterg*., 2014, **17**, 471–481. doi: 10.1007/s11743-014-1566-5
19. H. Gerengi, M.M. Solomon, S. Öztürk, A. Yıldırım, G. Gece and E. Kaya, Evaluation of the corrosion inhibiting efficacy of a newly synthesized nitrone against St37 steel corrosion in acidic medium: experimental and theoretical approaches, *Mater. Sci. Eng.: C*, 2018, **93**, 539–553. doi: 10.1016/j.msec.2018.08.031
20. M.J. Frisch, G.W. Trucks, H.B. Schlegel, G.E. Scuseria, M.A. Robb, J.R. Cheeseman, G. Scalmani, V. Barone, B. Mennucci, G.A. Petersson, H. Nakatsuji, M. Caricato, X. Li, H.P. Hratchian, A.F. Izmaylov, J. Bloino, G. Zheng, J.L. Sonnenberg, M. Hada, M. Ehara, K. Toyota, R. Fukuda, J. Hasegawa, M. Ishida, T. Nakajima, Y. Honda, O. Kitao, H. Nakai, T. Vreven, J.A. Montgomery, Jr., J.E. Peralta, F. Ogliaro, M. Bearpark, J.J. Heyd, E. Brothers, K.N. Kudin, V.N. Staroverov, R. Kobayashi, J. Normand, K. Raghavachari, A. Rendell, J.C. Burant, S.S. Iyengar, J. Tomasi, M. Cossi, N. Rega, J.M. Millam, M. Klene, J.E. Knox, J.B. Cross, V. Bakken, C. Adamo, J. Jaramillo, R. Gomperts, R.E. Stratmann, O. Yazyev, A.J. Austin, R. Cammi, C. Pomelli, J.W. Ochterski, R.L. Martin, K. Morokuma, V.G. Zakrzewski, G.A. Voth, P. Salvador, J.J. Dannenberg, S. Dapprich, A.D. Daniels, Ö. Farkas, J.B. Foresman, J.V. Ortiz, J. Cioslowski and D.J. Fox, *Gaussian 09, Revision C.01*, Gaussian, Inc., Wallingford CT, 2009.
21. N. Wazzan, I.B. Obot, H. Lgaz, Z. Safi and O. Al-Qurashi, Multiscale computational modeling of phytochemicals for iron corrosion inhibition: Bridging DFT, SCC-DFTB, and molecular dynamics for eco-friendly solutions, *J. Mol. Liq*., 2024, **406**, 125070. doi: 10.1016/j.molliq.2024.125070
22. I.B. Onyeachu, I.B. Obot, A.A. Sorour and M.I. Abdul-Rashid, Green corrosion inhibitor for oilfield application I: Electrochemical assessment of 2-(2-pyridyl) benzimidazole for API X60 steel under sweet environment in NACE brine ID196, *Corros. Sci*., 2019, **150**, 183–193. doi: 10.1016/j.corsci.2019.02.010
23. S. Öztürk, Synthesis and corrosion inhibition effects of quinazolin-(3*H*)-4-one derivatives containing long-chain pyridinium salts on carbon steel in 1.5 M HCl, *Prot. Met. Phys. Chem. Surf*., 2017, **53**, 920–927. doi: 10.1134/S2070205117050161
24. L.G. Qiu, A.J. Xie and Y.H. Shen, A novel triazole-based cationic gemini surfactant: synthesis and effect on corrosion inhibition of carbon steel in hydrochloric acid, *Mater. Chem. Phys*., 2005, **91**, 269–273. doi: 10.1016/j.matchemphys.2004.11.022
25. I. Aiad, M.A. Riya, S.M. Tawfik and M.A. Abousehly, Protection of carbon steel against corrosion in hydrochloric acid solution by some synthesized cationic surfactants, *Prot. Met. Phys. Chem. Surf*., 2016, **52**, 339–347. doi: 10.1134/S2070205116020027

26. X. Yang, J. Wang, Z. Ren and W. Hu, Preparation and corrosion resistance of Ni-Fe layer double hydroxides superhydrophobic film on carbon steel, *Colloids Surf., A*, 2023, **669**, 131501. doi: 10.1016/j.colsurfa.2023.131501
27. O. Mohamed, M. Hassan, M. Egilmez, W. Abuzaid, T. Ibrahim and M. Khamis, Corrosion behavior of CoCrNi/mild steel medium entropy alloy thin films, *Mater. Today Commun.*, 2022, **30**, 103015. doi: 10.1016/j.mtcomm.2021.103015
28. M.A. Amin, M.A. Ahmed, H.A. Arida, F. Kandemirli, M. Saracoglu, T. Arslan and M.A. Basaran, Monitoring corrosion and corrosion control of iron in HCl by non-ionic surfactants of the TRITON-X series - part III. Immersion time effects and theoretical studies, *Corros. Sci*., 2011, **53**, 1895–1909. doi: 10.1016/j.corsci.2011.02.007
29. N.A. Negm, N.G. Kandile, E.A. Badr and M.A. Mohammed, Gravimetric and electrochemical evaluation of environmentally friendly nonionic corrosion inhibitors for carbon steel in 1 M HCl, *Corros. Sci*., 2012, **65**, 94–103. doi: 10.1016/j.corsci.2012.08.002
30. S.A. Umoren and M.M. Solomon, Effect of halide ions on the corrosion inhibition efficiency of different organic species – a review, *J. Ind. Eng. Chem*., 2015, **21**, 81–100. doi: 10.1016/j.jiec.2014.09.033
31. E.K. Ardakani, E. Kowsari and A. Ehsani, Imidazolium-derived polymeric ionic liquid as a green inhibitor for corrosion inhibition of mild steel in 1.0 M HCl: experimental and computational study, *Colloids Surf., A*, 2020, **586**, 124195. doi: 10.1016/j.colsurfa.2019.124195
32. E. Ituen, O. Akaranta and A. James, Evaluation of performance of corrosion inhibitors using adsorption isotherm models: an overview, *Chem. Sci. Int. J.*, 2017, **18**, 1–34. doi: 10.9734/CSJI/2017/28976
33. C. Wang, C. Zou and Y. Cao, Electrochemical and isothermal adsorption studies on corrosion inhibition performance of β-cyclodextrin grafted polyacrylamide for X80 steel in oil and gas production, *J. Mol. Struct*., 2021, **1228**, 129737. doi: 10.1016/j.molstruc.2020.129737
34. S.S. Abd El Rehim, S.M. Sayyah, M.M. El-Deeb, S.M. Kamal and R.E. Azooz, Adsorption and corrosion inhibitive properties of P(2-aminobenzothiazole) on mild steel in hydrochloric acid media, *Int. J. Ind. Chem*., 2016, **7**, 39–52. doi: 10.1007/s40090-015-0065-5
35. Q. Zhang, Z. Gao, F. Xu and X. Zou, Adsorption and corrosion inhibitive properties of gemini surfactants in the series of hexanediyl-1,6-bis-(diethyl alkyl ammonium bromide) on aluminium in hydrochloric acid solution, *Colloids Surf., A*, 2011, **380**, 191–200. doi: 10.1016/j.colsurfa.2011.02.035
36. H.M. Abd El-Lateef, A.M. Abu-Dief, L.H. Abdel-Rahman, E.C. Sañudo and N.N. Aliaga-Alcalde, Electrochemical and theoretical quantum approaches on the inhibition of C1018 carbon steel corrosion in acidic medium containing chloride using some newly synthesized phenolic Schiff bases compounds, *J. Electroanal. Chem*., 2015, **743**, 120–133. doi: 10.1016/j.jelechem.2015.02.023

37. A.S. El-Tabei, M.A. Hegazy, A.H. Bedair, N. El Basiony and M.A. Sadeq, Experimental and theoretical (DFT&MC) studies for newly synthesized cationic amphiphilic substance based on a naphthol moiety as corrosion inhibitor for carbon steel during the pickling process, *J. Mol. Liq*., 2021, **331**, 115692. doi: 10.1016/j.molliq.2021.115692
38. A. Liu, H. Tian, W. Li, W. Wang, X. Gao, P. Han and R. Ding, Delamination and selfassembly of layered double hydroxides for enhanced loading capacity and corrosion protection performance, *Appl. Surf. Sci*., 2018, **462**, 175–186. doi: 10.1016/j.apsusc.2018.08.109
39. A. Yıldırım, S. Öztürk and M. Çetin, Novel amide-based cationic surfactants as efficient corrosion inhibitors for carbon steel in HCl and H_2SO_4 media, *J. Surfactants Deterg*., 2013, **16**, 13–23. doi: 10.1007/s11743-012-1356-x
40. S. Öztürk, H. Gerengi, M.M. Solomon, G. Gece, A. Yıldırım and L.O. Olasunkanmi, Synthesis, characterization, and studies of the interfacial and anticorrosion properties of a ternary cationic ionic liquid on carbon steel in a molar concentration of hydrochloric acid: Experimental and computational insights, *Colloids Surf., A*, 2024, **681**, 132720. doi: 10.1016/j.colsurfa.2023.132720
41. Y. Ji, B. Xu, W. Gong, Z. Zhang, Z. Jin, W. Ning, Y. Meng, W. Yang and Y. Chen, Corrosion inhibition of a new Schiff base derivative with two pyridine rings on Q235 mild steel in 1.0 M HCl, *J. Taiwan Inst. Chem. Eng*., 2016, **66**, 301–312. doi: 10.1016/j.jtice.2016.07.007

♦ ♦ ♦